DETERMINING MEAN CORPUSCULAR HEMOGLOBIN FROM A DROP OF BLOOD USING CONTACT OPTICAL MICROSCOPY

by

Hershel Simon Guzner Macaulay

Submitted in partial fulfillment of the requirements
for the degree of Master of Applied Science

at

Dalhousie University
Halifax, Nova Scotia
March 2015

To my family

Table of Contents

List of Tables

List of Figures

Abstract

Mean corpuscular hemoglobin (MCH) measures the average hemoglobin per red blood cell, and is a component of the complete blood count (CBC), a common panel of several basic and clinically important blood parameters. Contact optical microscopy (COM) is a novel and highly compact imaging technology that has the potential to deliver a point-of-care CBC, which could strongly impact many fields of medicine. In this research, it was hypothesized that by using COM, MCH can be measured as a component of a CBC, with clinically acceptable accuracy and precision, from a drop of blood.

A COM-based system was built to test the hypothesis. A microspectrophotometry equation and a computer-vision algorithm were developed to extract the MCH from COM images of films of blood containing intact red blood cells. The MCH of 15 human blood samples from different subjects was measured using both a standard-of-practice Sysmex XN-10 CBC machine and the COM system. Regression analysis was used to quantify the performance of the COM system in relation to the standard of practice. An R^2 of 0.89 was obtained, showing good correlation between the COM system and the standard of practice. A coefficient of variation of 4.0% was obtained, surpassing the clinical target of 5%. The results showed that MCH can be measured precisely using COM-based microspectrophotometry and suggest that there is potential for further precision gains.

List of Abbreviations and Symbols Used

CBC	Complete blood count
CMOS	Complementary metal-oxide semiconductor
COM	Contact optical microscopy
Deoxy-Hb	Deoxygenated hemoglobin
DIH	Digital inline holography
EDTA	Ethylenediaminetetraacetic acid
Hb	Hemoglobin
Hb_p	Moles of Hb above a COM pixel
Hgb	Mass of Hb per volume of blood (CBC parameter)
LED	Light-emitting diode
FWHM	Full-width at half maximum
MCH	Mean RBC corpuscular hemoglobin (CBC parameter)
MCHC	Mean corpuscular Hb concentration (CBC parameter)
MCV	Mean corpuscular RBC volume (CBC parameter)
Met-Hb	Methemoglobin
OV8850	The COM sensor used in this research
Oxy-Hb	Oxygenated hemoglobin
[Platelet]	Platelet concentration (CBC parameter)
POC	Point-of-care
RBC	Red blood cell
[RBC]	Red blood cell concentration (CBC parameter)
RDW	RBC volume distribution width (CBC parameter)
StP	Standard-of-practice CBC machine
WBC	White blood cell
[WBC]	White blood cell concentration (CBC parameter)
a	Slope of regression line
b	Y-intercept of regression line
C	Concentration
CV	Coefficient-of-variation
$CV_{precision}$	CV of the error of a measurement
CV_{total}	Estimate of COM's $CV_{precision}$ of a CBC parameter
$CV_{MCH,total}$	CV_{total} for the MCH parameter
CV_{count}	CV of counting error
$CV_{MCH,\varepsilon}$	CV of MCH error independent of experimental subject
$CV_{MCH,h}$	CV of MCH of experimental-subject random effect
$CV_{MCH,person}$	CV of MCH error due to a specimen's COM characteristics
CV_{StP}	CV of the StP for a CBC parameter
$CV_{MCH,StP}$	CV_{StP} for MCH
$CV_{MCH,sampling}$	CV of RBC sampling error for MCH
CV_{target}	The clinical target for CV_{total}, $CV_{precision}$ for a CBC parameter
$CV_{MCH,target}$	CV_{target} for MCH
D	Dilution factor
d	Pixel side-length
ϵ	Coefficient of extinction

h	Statistical random effect
I	Transmitted light intensity
I_p	Estimated transmitted light intensity for a pixel
I_0	Incident light intensity
$I_{0,p}$	Estimated incident light intensity for a pixel
i	Specimen number
j	Test number for a particular specimen
ℓ	Path-length
M_{Hb}	Molar mass of Hb
m_{Hb}	Mass of Hb
$m_{Hb,p}$	Mass of Hb above a COM pixel
$m_{Hb,RBC}$	Mass of Hb in an RBC
n	RBC index when counting
N	Total number of RBCs
p	Pixel index within an RBC
P	Number of pixels in an RBC
r	The ratio of Hb's and water's refractive indices
R^2	Coefficient of determination
V	Volume
$\alpha_{scattering}$	Scattering coefficient
ε	Regression residual
λ	Wavelength
σ	Standard deviation

Acknowledgements

I am grateful to my supervisor, Alan Fine, for giving me the opportunity to conduct this research, and for the guidance, patience, enthusiasm, and support that allowed me to complete it. I would also like to thank my co-supervisor Peter Gregson for his wisdom and guidance, as well as committee members Drs. Paul Gratzer and Ian Hill.

This research was the result of a strong team effort, and would have been impossible without the advice, assistance, and hard work of several people. From the Fine lab, I would like to thank: Alexander Goroshkov, George Kitching, Ranga Rankaduwa, Yiling Hu, and Uli Hoeger. From Alentic Microscience Inc, I would like to thank: Noah Hymes-Vandermulen, Stephanie Murray, Ed Gregson, and Albert Casha. From Dalhousie University, I would like to thank: Drs. Rob Liwski, Thomas Trappenburg, and Ted Hubbard. Special thanks go to Michal Lisicki for helping with the MATLAB code, Dr. David Hamilton for helping with the mixed-model statistical analysis, and Maria Rosario Reyes for help with the R code. I would also like to thank Dr. David Conrad for providing the blood samples and standard-of-practice measurements.

I am thankful to the professors and administrators in the Department of Biomedical Engineering for the excellent education I received in this Master's program. I am also thankful for personal or research support from the following funding agencies: NSERC, CREATE Biomedic, ACOA, CIHR, and Innovacorp.

Finally, I would like to thank my friends, classmates (current and past), brothers, cousins, and of course my parents, for your love, company, and support.

Chapter 1: Introduction

1.1: Background

Point-of-care (POC) diagnostics is an increasingly important approach to medical diagnostics with the potential to revolutionize healthcare delivery. In the developed world, healthcare accounts for a large proportion of economic expenditure (12% of gross domestic product in Canada in 2012[1]) and requires significant time, energy, and financial expenditure for patients. Delays in healthcare delivery can compound ailments, a problem exacerbated in remote and less economically developed regions of the world, where access to any healthcare may be limited. POC technology that can enable rapid and reliable diagnosis and monitoring of patients' health conditions, in any setting, using handheld, non-invasive, low-cost devices[2], may have a major impact on healthcare delivery.

One of the most commonly used medical tests that could benefit from POC technology is the complete blood count (CBC). The CBC is a compilation of several basic blood analyses that assist a medical practitioner in the initial determination of general health and guide the next steps in the diagnostic process. For example, the CBC can indicate infection (including potential classification, i.e., bacterial versus viral), anemia (a common cause of fatigue, dizziness, etc.), thrombocytopenia (reduction in platelets with associated impaired hemostasis), immune disorders, and can help discriminate many other conditions[3].

CBCs are ordered in many medical settings, such as general practitioners' offices, emergency rooms, remote locations, and medical wards. Current standard-of-practice (StP) CBCs are performed on a vial of venous blood, typically with several potentially expensive steps and up to several days delay between ordering the test and acting on the results, including phlebotomy (often at a separate location from test requisition) and delivery of the blood to a central laboratory for measurement using a large StP machine. Also, venipuncture can be painful, particularly when a vein is hard to find.

A POC device able to perform a CBC on a drop of capillary blood, drawn with a lancet, would therefore expedite the process significantly and make it more comfortable for patients. The goal of this research is to contribute to proving the concept for performing a CBC on a drop of blood using contact optical microscopy (COM), a new technology with the potential to enable a handheld, POC device.

1.1.1: CBC Parameters

The CBC measures the properties of the three main blood-cell types: red blood cells (RBCs), or erythrocytes; white blood cells (WBCs), or leukocytes; and platelets, or thrombocytes. There are several independent parameters measured in a CBC:

1) MCH: mean corpuscular hemoglobin (Hb), i.e., the average mass of Hb per RBC
2) [RBC]: RBC concentration (Note: "[X]" indicates concentration of "X")
3) MCV: mean RBC volume
4) RDW: RBC volume coefficient of variation (CV)
5) [WBC]: WBC concentration
6) [Platelet]: platelet concentration

There are 3 clinically useful Hb-related parameters obtained in a CBC: MCH, Hgb (the mass of Hb per volume of blood), and MCHC (Mean corpuscular Hb concentration, i.e., the average Hb concentration per cell). Given any one of the three Hb measures, as well as [RBC] and MCV, the other two can be calculated directly. Other combinations of the 6 core measures are used clinically, such as the hematocrit, which is the volume fraction of RBCs in blood, calculated as the product of [RBC] and MCV. The focus of this research in particular is to measure the MCH, but within the context of a system that could potentially measure all the CBC parameters.

An extended test, the CBC with differential (CBCD), finds all the above parameters and also differentiates the types of WBCs to some extent. The subtypes of WBCs, in order of decreasing percentage in normal individuals are:

1) Neutrophils (40-65%)
2) Lymphocytes (20-40%)

3) Monocytes (2-10%)
4) Eosinophils (1-4%)
5) Basophils (<1%)

Neutrophils and lymphocytes, the most common subtypes, are generally the most important WBCs diagnostically. Among other things, their elevated concentrations may be indicative of bacterial and viral infections, respectively. However, WBC classification, while of interest to the Fine lab, is outside the scope of this research.

1.2: Design Requirements for Diagnostic Usefulness

1.2.1: POC Design

A POC CBC machine might be deployed in a wide variety of contexts. Users' needs and the design requirements that are necessary to meet them are likely to vary between contexts, potentially requiring separate designs. Nevertheless, a broad set of capabilities and attributes can be defined for POC devices.

The device must achieve the accuracy and precision requirements needed to allow clinicians to make relevant diagnostic decisions in the setting in which it is to be used. Both the devices and the tests performed with them must be of relatively low cost, for such devices must be distributed to many doctors' offices and still be competitive with high-throughput, central-lab systems on a test-to-test basis. Due to space constraints in a portable device for subsystems that automate experimental steps (such as the mixing of blood samples with reagents), more manual steps may be required, and the impact of possible human error should therefore be mitigated[2].

So as not to waste the physician's or patient's time while waiting for a result, a full POC testing procedure should take at most a few minutes. This includes the whole process of opening any disposable components, drawing blood, mixing it with any reagents or diluents required, loading the sample into the device, conducting the test, cleaning the device, and disposing of the waste when the test is finished. This whole process must furthermore be safe for the user and leave the device uncontaminated. An example of an

effective POC test is a pregnancy test, which is so easy to perform that a consumer can use one right out of the box.

To set design targets for this proof-of-concept research, the ultimate use of the test should be considered. A physician needs to be able to make useful decisions using the information available. These decisions are made based on a combination of test results, the patient's signs and symptoms, the patient's history and physical examination, and the context (e.g., there may be an ongoing flu epidemic). These factors create a set of *a priori* probabilities for particular medical conditions. If appropriate, these *a priori* conditions can lead to a CBC being requested by a physician to help specify or increase confidence in an eventual diagnosis. The CBC results may alter these probabilities, leading to a particular diagnosis or to follow-up tests. In this situation, the accuracy and precision of a POC device affects how much credence the clinician can put on the results, and thus how much the *a priori* probabilities should be modified. Clearly, this determines the usefulness of the device's output.

1.2.2: Range & Correlation

Table 1 shows several relevant parameters that help define and interpret clinical accuracy, precision, and range requirements for a CBC. Examples of normal reference ranges for CBC parameters are shown in Column 2, representing the typical ranges a given subpopulation might exhibit. Subpopulations can be best established on the basis of age, sex, ethnicity, work history, locale, etc[3]. Column 3 shows the outer limits of multiple sources for the reference range. This outer range is important for designing a device that must provide reliable results for any healthy subpopulation, and it is therefore designated as the "required range" for this research. The other columns from Table 1 are described below.

Table 1: CBC Requirements

1 **Measure**	2 **Sample Ref. Range** [3]	3 **Required Range** [3],[4],[5]	4 **CV_{StP} (%) (2008)** [6]	5 **CV_{target} (%): Buttarello** [6]	6 **CV_{target} (%): Beck** [3]
Hgb	13.8-18.0 g/dL	13.0-18.0 g/dL	<2.0	4	5-10
MCV	80-99 fL	78 – 100 fL	<2.0	2	5-10
RDW	11.6-14 %	10.0 - 14.5 %	<2.0	3	5-10
[RBC]	4.8-5.8 $*10^3$ /nL	3.5-6.0 $*10^3$ /nL	<1.0	4	5-10
[Platelet]	150-400 /nL	150-400 /nL	<5.0	6	5-10
[WBC]	4-10 /nL	3.5-12 /nL	<2.0	17	5-10
MCH	27-31.5 pg	24 – 37 pg	<2.0 [7]	N/A	5-10

A clinical device would also have to perform satisfactorily outside the required range when patients have abnormal blood, so the required range here is not necessarily a conservative target. However, atypical values are outside the scope of this proof-of-concept research.

1.2.3: Accuracy & Precision

Diagnostic accuracy, the definition of accuracy used in this research, refers to the level of agreement between a measurement result and the reference value. According to ISO 15725-1, accuracy refers to a combination of precision and bias/trueness[8]. Bias is the difference between the reference value and the mean of a large number of measurements made at that reference value, which could vary over the measured range. (The term accuracy can also refer to the difference of the mean from the reference value, but this definition is not particularly helpful when evaluating a diagnostic device.) Note that an imaginary, perfectly calibrated device has zero bias over the whole required range, so accuracy becomes equivalent to precision.

Precision is the degree of agreement of the results of multiple measurements made at the same value of an independent variable. This research refers to precision in terms of coefficients-of-variation (CVs). The CV of a series of measurements is equal to their standard deviation divided by their mean, multiplied by 100. To simplify device

evaluation, precision requirements are expressed here as a single CV value for each CBC parameter. $CV_{precision}$ is approximated here as

$$CV_{precision} = \frac{\sigma_{precision}}{\overline{StP}} * 100 \quad (1)$$

where $\sigma_{precision}$ is the standard deviation of the calibrated measurements, and $\overline{StP}$ is the mean of the reference values for the parameter in question. Note that if the range of the reference values is too wide, or $\sigma_{precision}$ varies excessively over this range, this simplified definition of $CV_{precision}$ would not be sufficient, and a reference value-dependent definition would be needed.

Measurement instruments can be calibrated, which means that unless there is significant instrument drift, precision is more important than accuracy. For this proof-of-concept research, therefore, $CV_{precision}$ is the most relevant performance criterion. $CV_{precision}$ must not exceed its design target, referred to as CV_{target}.

1.2.4: Defining CV_{target}

Ultimately, clinical design requirements for a commercial medical test must be satisfactory from a marketing and regulatory perspective. Recommendations from leading physicians in relevant medical fields are essential, and device performance indistinguishable from the StP (in terms of range, accuracy, and precision) may be an efficient route to obtaining such recommendations, assuming other POC-specific requirements are met. Typical accuracy characteristics of commercial StP machines are shown in Table 1, Column 4.

The StP machine used in this research, for example, has a CV_{StP} of < 2% for MCH. However, the purpose of this research was to develop a candidate approach for POC-CBC analyses and demonstrate its potential, so a $CV_{MCH,target}$ of 2%, while ideal, was not required for this research. As shown in Table 1, StP machines tend to report much better performance than is clinically necessary[6]. Therefore, this section seeks to define less stringent but still clinically relevant design targets for precision.

In the context of how the CBC is used practically, there are two basic needs for the measurement. First, the measurement should be accurate enough to indicate if a patient's CBC parameters are inside, above, or below the respective reference ranges. The uncertainty in the measurement should be small so that measurements close to the reference-range limits can be classified as normal or abnormal with adequate reliability. Second, when monitoring a patient over time, the measurement should be precise enough that it is clear if the patient's values have changed beyond their natural variation. This second need requires a smaller CV_{target}[6].

Given the above, one approach to defining CV_{target} is to identify a "usefulness limit" beyond which natural biological variations become the primary source of error on a patient's mean value. Based on natural diurnal (day-to-day) variations, Buttarello calculates requirements for $CV_{precision}$[6], shown in Table 1, Column 5. However, Buttarello does not clearly state how he arrived at these numbers so it is difficult to interpret them. Also, Buttarello does not provide an explicit CV_{target} for MCH.

Beck's opinion (Table 1, Column 6) on the matter is less restrictive in most cases[3]. The error and potential biases associated with real-world scenarios are higher than those reported by hematology-analyzer manufacturers. This is because the entire testing process has several sources of error. Phlebotomy can affect results, as can the operator of the analyzer, the amount of time between blood draw and measurement, calibration of the StP machine, etc. Beck recommends: "…generally one cannot infer that serial results mean anything unless they are, in most cases, at least 10–15% apart – sometimes up to 20% apart"[3]. To ensure that measurements with 10-20% separation are statistically distinguishable (two standard deviations apart), the $CV_{precision}$ of the entire testing procedure should be ½ of this proposed interval, i.e., 5-10%. Given this reality, even if results do not meet Buttarello's criteria, they would not necessarily be unacceptable from a medical standpoint.

The entire testing process is necessarily considered when evaluating the $CV_{precision}$ for a POC device. Matching the real-world precision for typical, StP CBCs is therefore a useful target for this research. The exact value within the 5-10% range may depend on

the particular parameter in question and the medical context, so for this research, the conservative value of 5% is designated as the $CV_{MCH,target}$.

Note, though, that when MCH and [RBC] are measured directly while Hgb is calculated as a product of the two, in order to achieve $CV_{Hgb,precision} = 5\%$, both $CV_{MCH,precision}$ and $CV_{[RBC],precision}$ would have to be smaller than 5%. The exact requirement for $CV_{MCH,precision}$ would depend on what is achievable for $CV_{[RBC],precision}$ in the POC device, which is currently unknown. If, for example, the $CV_{MCH,precision}$ is half of the 5% $CV_{Hgb,target}$, then the effective $CV_{[RBC],precision}$ requirement would be $\sqrt{5\%^2 - 2.5\%^2} = 4.3\%$ (this value could be even smaller if there is a correlation between MCH and [RBC]). Further reduction of $CV_{MCH,precision}$ would have diminished returns in this case. Therefore, although 5% is used as the $CV_{MCH,target}$ for this research, achieving $CV_{MCH,precision}$ as low as 2 or 3% may be necessary, depending on what is achievable for [RBC]. A similar argument applies when calculating the MCHC, which requires dividing the MCH by the MCV.

1.3: CBC Measurement Approaches

1.3.1: Coulter Counter (StP)

At present, StP CBCs are usually performed via Coulter counters, machines with several different subsystems for making different measurements on the blood. Blood samples are chemically processed and then the cells are made to flow rapidly in single file through tubes with impedance and/or optical detectors that count, size, and classify the cells. Hb is detected in a separate part of the machine using optical spectroscopy on lysed RBCs. Standard Coulter counters are large, expensive, benchtop machines, which makes them unsuitable in POC contexts.

1.3.2: Microfluidics

Two general strategies have been employed in the literature in attempts to demonstrate a POC CBC. The most common strategy is to try to miniaturize the Coulter counter using microfluidic technologies. These approaches typically use impedance-based cell measurement and employ intricate microfluidic channels fabricated on tiny chips.

However, such devices are complex and must integrate many components, such as reservoirs, pumps, optics, electronics, fluidics, impedance sensors, etc., making them difficult to scale down into a useful POC device[9]. Much progress has been made[9]–[12], but there have been no reports to date of a full CBC using microfluidics.

1.3.3: Automated Blood Imaging

The other main strategy is automated blood imaging, which is the technique used in this research. In imaging strategies, images are taken of a blood film containing many cells using a microscope, and computer-vision algorithms are used to extract the CBC parameters from these images. Though these strategies cannot easily take advantage of impedance measurements, microscopy systems produce morphological information that simple microfluidics systems cannot.

When a blood film is imaged such that the cells are resolvable, [RBC], [WBC], and [Platelet] can be measured by segmenting, classifying, and counting each cell type in the field of view. The concentration of cells in a fluid is given by

$$C = N * D/V \tag{2}$$

where N is the number of cells counted, V is the volume of the imaged blood film, and D is the dilution ratio if the sample was diluted before imaging.

MCV and RDW could potentially be measured by calculating the mean and the standard deviation of the areas in an image covered by RBCs and then applying a correction factor to convert these areas to volumes. Prior to this research, hemoglobin has typically been measured in a separate sample-processing step by lysing the RBCs and performing a standard spectrometric measurement, yielding Hgb[13].

Current Imaging Drawbacks & Limitations

When not using a Coulter counter, the concentration of cells is normally measured using a standard, lens-based microscope and a hemocytometer as the specimen chamber. There are several drawbacks to this kind of system in a POC context, even if automated. Optical microscopes typically are too large and heavy for POC use since they typically

must consist of light sources, two or more lens groups, focusing and alignment mechanisms, long light paths, and stable bases.

Even when microscopes can be miniaturized, there is still the major challenge that resolution tends to decrease with increasing field of view. This tradeoff affects the precision of the cell-concentration parameters in a CBC. Uncertainty in each of the terms in Equation (2) can contribute error to C. One component of the error on N is the error due to counting statistics, equal to the square root of the expected value of the count. Thus, for sufficiently large N, $e_{\mathrm{count}} \approx \sqrt{\mathrm{N}}$, where e_{count} is the error due to counting statistics, and $\mathrm{CV}_{\mathrm{count}} \approx 100/\sqrt{\mathrm{N}}$, where $\mathrm{CV}_{\mathrm{count}}$ is the contribution of counting error to $\mathrm{CV}_{\mathrm{precision}}$. $\mathrm{CV}_{\mathrm{count}}$ is reduced by counting more cells. One of the challenges for image-based, POC-CBC design is obtaining the needed WBC counts in the field of view while preventing RBCs, which are typically at ~1000x higher concentration, from overlapping in the image. If blood is diluted such that the RBCs cover half of the field of view of an image of stationary cells, a total field of view of ~10 mm^2 is typically required to obtain a $\mathrm{CV}_{[\mathrm{WBC}],\mathrm{count}}$ of 10% (i.e., 100 WBCs counted). However, a standard microscope cannot resolve cells at a magnification corresponding to such a large field of view.

Some groups have dealt with these problems using a combination of compact optical design and a scanning objective lens to increase the field of view. For example, Hemocue sells a WBC-differential device[14] that could be considered to be POC. However, such approaches are not easily extensible to counting or sizing RBCs, as they rely on lysing the RBCs. Lysing allows them to load blood into a thicker specimen chamber, increasing the total volume and therefore the WBC counts, and then letting the WBCs settle by gravity into optical focus on the lower chamber surface. Had the RBCs not been lysed, cells would stack on top of each other, becoming unresolvable.

A crude way to perform the different CBC measurements in a smaller field of view is to sequentially load separate specimen chambers and blood preparations into the imager, each designed to measure different CBC parameters. Ozcan and collaborators have demonstrated this concept by using an intact cellphone camera coupled to miniaturized optics to create a very compact device[13]. Their approach required three separate

specimen chambers (for RBC count, WBC count, and hemoglobin spectroscopy) that each had to be loaded with separate blood preparations and slid into place in the device, one after the other. This would not be convenient in a POC context. An imaging device would likely be smaller, faster, simpler, and cheaper if it could measure all the CBC parameters in a single step.

1.3.4: Lensless Microscopy

Lensless optical microscopy may solve many of the problems noted above. Lensless microscopy is an exciting, developing field with the potential to bring cheap, compact, large-field-of-view microscopes into POC contexts. When the image of an object is projected onto an image plane without any intervening lenses, this is known as a shadow imaging. The edges of the image are blurred due to diffraction, decreasing image resolution. When imaging cells, the resulting resolution is insufficient[15]. There are two techniques that have been used to overcome this loss of resolution in large-field-of-view lensless microscopy[16]. These are digital inline holography (DIH) and contact optical microscopy (COM), compared in Figure 1.

Digital Inline Holography

DIH, pioneered by Jericho and Kreuzer[17] uses a coherent light source (an LED behind a pinhole) and snaps a shadow image of a microscopic sample held >100 μm above an optical sensor array[15]. Because the light is coherent, the diffracted light interferes with undiffracted light at the image plane, creating rings known as interference fringes. These rings contain spatial information about the refractive index of the sample, and thus appropriate algorithms can use these fringes to reconstruct an image of the original sample[15].

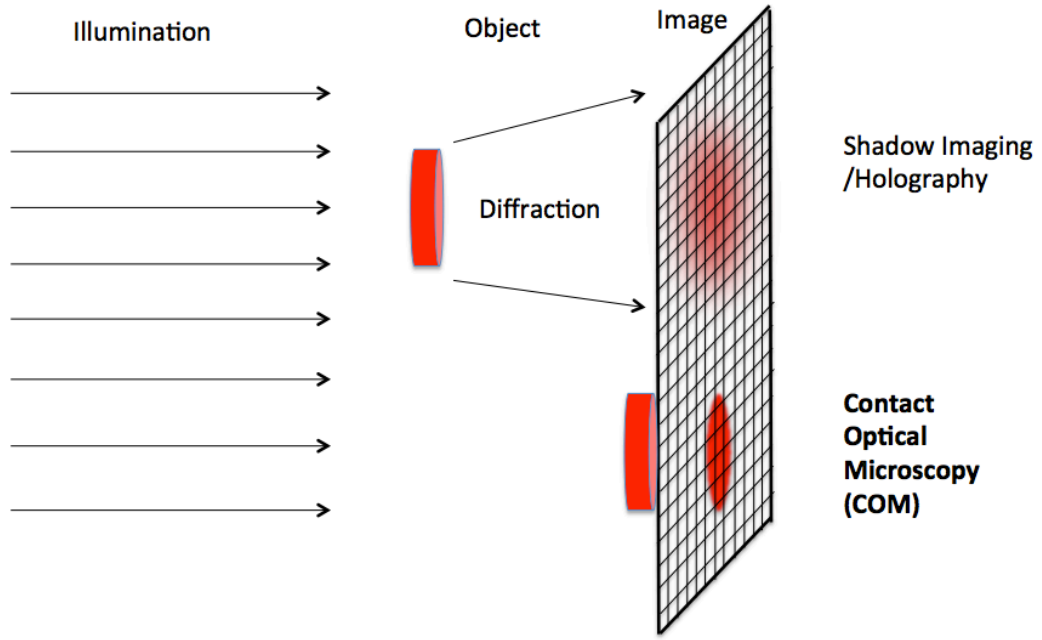

Figure 1: Comparison of shadow imaging, DIH, and COM. Note that DIH requires coherent light and that the resulting raw image would contain interference fringes.

Contact Optical Microscopy

The other main lensless microscopy technique is COM, the subject of this research. This technique has been in development since 2003 by Alan Fine, the supervisor of this research. To avoid diffraction-induced resolution reductions, COM relies on the object being in direct contact with the image sensor. As a result, when light diffracts at an objects' edge, there is no appreciable distance over which the light spreads, just as the edges of a shadow become more defined when the object is brought toward its shadow.

In COM, the image plane is an imaging sensor array, and the resolution of COM is determined for the most part by the pixel size. Modern cellphone cameras, in the quest for miniaturization, now employ pixels of side length as small as 1 μm. Such pixels can resolve many cell types. Sensors with over 5 million pixels and fields-of-view of 10 mm^2 and higher are now available. DIH benefits similarly from decreased pixel size and increased fields of view of camera sensors.

Fine's lab has been exploring blood-imaging applications of COM, and has made developments toward a POC CBC, using the general principles stated previously for extracting the non-Hb CBC parameters from an image of a blood film.

Previous Efforts Towards Lensless Microscopy

COM has also been attempted by others. Efforts by Abshire suffered from poor resolution[18], and this approach appears to have been abandoned by that group. Ohta's group perused COM as well, but their sensors also had low resolution and were unable to resolve cells[19].

Yang and collaborators at Caltech used a commercially available complementary metal-oxide-semiconductor (CMOS) image sensor with pixel-size of 2.2 μm to detect RBCs. They further applied so-called "superresolution" algorithms[20] to improve the resolution beyond the pixel-size limit[21]. This involves illuminating the sample sequentially from multiple angles, causing sub-pixel shifts of images. These images are then algorithmically reconstructed into a higher resolution image, allowing for visualization of internal cell features[21].

Yang's group employed a different technique to image cells flowing in a microchannel, using cell movement and a fixed illumination angle to generate subpixel shifts[22]. They used this approach along with a vital stain and sequential multicolour illumination to identify malaria plasmodia in RBCs[23]. However, this was performed on a purified RBC population because WBCs were too large to flow through their microchannel. A microchannel would have to be at least 10 μm high to allow unconstrained WBC flow, but this may leave some RBCs off the surface and blurred, similar to being out of focus on a standard microscope.

Ozcan and collaborators have worked with DIH, and have similarly applied angle shifts of the illumination in order to create multiple low-resolution holograms that are reconstructed into a high-resolution image. They have demonstrated imaging a thin blood smear (a one-cell-thick film of blood that is dried onto a transparent slide and stained) with sufficient resolution to resolve the nucleus of WBCs and perform basic

differential classification[24]. However, this has not been demonstrated in the quantitative fashion required for obtaining CBC parameters.

Neither COM nor DIH have yet been reported to perform a full CBC, as there are drawbacks to both. The cost of the sensors, along with the surrounding fluidics and hardware, may preclude a fully disposable device, at least where low-cost applications such as the CBC are intended. However, the sample must be placed very close to the sensor, meaning the sensor likely needs to be cleaned after each test, increasing the complexity. DIH, on the other hand, imposes a time delay because of the computation required to reconstruct the original image. It also has difficulty reconstructing densely packed samples, though dense packing is essential for statistically valid counts of both RBCs and WBCs from static images. To solve this problem, Ozcan has described z-plane shifting, i.e., acquiring multiple images at different sample-to-sensor distances, but this adds complexity to the device and further increases image-acquisition and processing time[16]. Nonetheless, both methods seem promising for blood-analysis applications. While Ozcan's group appears to be pursuing blood analysis with holography, no research groups or companies other than Fine's laboratory appear to be actively pursuing a COM-based CBC, despite its game-changing potential.

Microspectrophotometry for Hb Measurement

A particular area that has not been addressed in recent literature, either for COM or DIH, is how to obtain Hb measurements from a blood image without lysing the RBCs. As a result, POC-CBC schemes typically require a separate spectroscopic subsystem to measure Hb, in which the RBCs are lysed. This adds bulk and complexity to the process, negating some of the benefits of POC imaging.

This research introduces COM-based microspectrophotometry. In this technique, light-absorbing molecules contained in the volume between a light source and individual COM pixels are quantified using optical-absorption measurements. As discussed in Chapter 2, COM itself may have advantages over other microspectrophotometry systems. COM-based microspectrophotometry is hypothesized to enable measurement of the Hb content of individual RBCs in an image. This could then be averaged over all the RBCs available

to estimate the MCH. With the MCH, along with MCV and [RBC], also hypothesized to be extractable from a COM image, MCHC and Hgb could be derived, completing the CBC.

Given the gap in the literature, and the potential benefits of microspectrophotometry, the focus for this research was chosen to be Hb measurement using COM, specifically the MCH.

1.4: Central Hypothesis

Using COM, the MCH can be measured as a component of a CBC, with clinically acceptable accuracy and precision, on a drop of blood.

1.4.1: Scope

Within Scope

The scope of this research includes the development of a method used to extract an MCH measurement from a COM image. This includes the derivation of a mathematical equation for MCH and a basic computer-vision algorithm to extract the required inputs for the equation. Development of an illumination system by which to take the images is also included. The scope features an experiment in which COM and StP values for the MCH are compared statistically across several human subjects in order to test the performance of the system. Establishment of limitations and failure modes of the above is within the scope.

Outside Scope

The development of the COM imager itself and the initial conceptualization of the displaceable chamber lid (see Chapter 3) was performed by others prior to this research. Development of the displaceable chamber-lid system was conducted by the author but is not in the scope of this research.

Optimization of experimental parameters is outside the scope of this research except to the extent required for the concept to be demonstrated. Likewise, computer simulation of

system components is excluded. Though limitations of the computer-vision algorithm are explored, optimization and comparative analysis of algorithms is outside the scope.

Measurement of abnormal MCH values is outside the scope of this research. Validation of the repeatability requirements when building multiple COM systems was outside of the scope of this work; rather, demonstrating functionality in one device was deemed sufficient. Scalability of manufacturing of the device was also outside the scope. User experience of the device in a medical context was outside the scope of the hypothesis.

1.4.2: Intellectual Contributions

COM, the central hypothesis, and the general research focus were developed by Dr. Fine, the supervisor of this research. Dr. Fine also conceived of the general approach to COM-based blood imaging used here, and the general approach for experimentation. He also suggested microspectrometric hemoglobin quantification, including conversion to methemoglobin via nitrite, as a possibility for MCH measurement.

The intellectual contributions of the author include the approach for calculating the MCH using COM-based microspectrophotometry and the computer-vision algorithm for generating the results. Many aspects of the experimental apparatus, design, and procedure were designed by the author. The statistical analysis was contributed by the author based on guidance from Dr. David Hamilton and Maria Reyes. The contents of the discussion and many of the final recommendations were contributed by the author.

1.4.3: Summary of Chapters

Chapter 1 develops the case for using COM to implement a device capable of performing POC CBCs, and introduces the central hypothesis and scope of the work described herein. The clinical performance targets are discussed, and the various approaches for obtaining a POC CBC are discussed.

Chapter 2 summarizes the key literature related to microspectrophotometry. It then develops a mathematical method for obtaining an MCH measurement from a COM image. The assumptions and limitations of this approach are discussed, and experiments are proposed to test the validity of the method. The case is made for converting Hb to a

modified form, met-Hb, prior to measurement, to negate the potentially confounding effects of Hb oxygenation.

Chapter 3 describes the experimental methods used to test the central hypothesis. The chapter describes the blood diluent, the COM sensor, the optical system, the mechanical system, the experiment designs for three experiments, the testing protocols, the computer-vision algorithm for measuring MCH, and the statistical methods used for analysis. In Experiment 1, the MCH of 15 subjects is measured multiple times for each subject using COM and met-Hb conversion. The results are regressed against the StP measurement for each subject. In Experiment 2, 6 subjects are tested, with and without met-Hb conversion. Experiment 3 tests the change in MCH as measured by COM in one of the subjects after a three-day *ex vivo* blood incubation.

Chapter 4 presents the results of each of the three experiments as compared to the performance targets.

Chapter 5 discusses the results and their support of the central hypothesis. Experiment 1 supported the central hypothesis, though with room for improvement and further confirmation. Experiment 2 indicated that met-Hb conversion had little effect, though this could have been due to the experimental procedure. Experiment 3, along with observations from within Experiment 1, indicate that the COM-measured MCH can be reduced by changes in RBC morphology. The source of these changes is discussed. The limitations of the computer-vision algorithm are discussed, as are the limitations of the system design and experimental protocols.

Chapter 6 draws conclusions, most importantly that the central hypothesis was supported by this research, and makes recommendations for future work.

Chapter 2: Microspectrophotometry for Hemoglobin Measurement

2.1: Microspectrophotometry Literature

To calculate the MCH from a COM image, microspectrophotometry must be used to quantify Hb content. Microspectrophotometry within lens-based microscopy has existed for many decades and has been performed previously on RBCs. In 1960, Sondhaus & Thorell published a study in which the Hb absorbance spectra from sub-areas of RBCs were examined, exploring the correlation of RBC maturity and Hb and free-iron content[25]. Tsujita *et al* measured the change of the absorbance spectrum within RBCs depending the presence of nitric oxide[26].

In 1985, Meletis *et al.* attempted to measure MCH using lens-based transmission microspectrophotometry[27]. They sampled blood from pregnant women using venipuncture, lightly centrifuged the sample and then redispersed the cells at 10:1 dilution. A sample was then formed into a smear on a glass slide. In each sample, 50-100 RBCs were measured by illuminating them with 415 nm light, dividing the full area of each RBC into 0.5 μm pixels, and measuring absorbance at each pixel. The process took 60-90 minutes per test. Using MCH_{StP} values ranging from 16-36 pg, this experiment yielded a linear correlation with the StP of $R^2 = 0.87$ and $CV_{MCH,precision} = 28\%$. R^2 is a measure of correlation, discussed further in section 3.2.7. The R^2 value close to 1 indicates that microspectrophotometry is a reasonable method for MCH measurement. However, the $CV_{MCH,precision}$ value is well over the $CV_{MCH,target}$ of 5%. It is not clinically acceptable as there can be little confidence that a measurement falling inside the reference range represents a normal or an abnormal true value.

Some of this deficiency might be assigned to 1985 technology and small RBC sample sizes. In COM on the other hand, large numbers of RBCs can be readily available for measurement. Lens-based microspectrophotometry for quantification of absorbing molecules is also sensitive to focal plane alignment relative to the RBCs, since light transmitting through Hb that is outside the focal plane may not be collected. The depth of focus of the objective lens used in the above experiment was ~0.4 μm[28], which is much thinner than an RBC (typically 1.1 μm thick at the center and 2.6 μm thick at the torus-

shaped outer band[29]), meaning parts of every RBC measured were out of focus. This could have resulted in part of the Hb signal being blurred outside the cell borders and lost. COM, on the other hand, has no focal plane – COM produces very little blurring of objects less than a few microns from the imaging surface[18]. With COM's advantages, there was potential for COM to outperform standard microspectrophotometry at MCH measurement.

2.2: MCH Calculation

Standard optical spectrometry measures the quantity of a light-absorbing analyte dispersed in a solution using Beer's law[30]:

$$\frac{I}{I_0} = 10^{-\epsilon C \ell} \tag{3}$$

where I_0 is the incident light intensity, I is the transmitted light intensity, ϵ is the extinction coefficient of the absorber (Hb in this case) at the incident wavelength, C is the concentration of the absorber in the solution, and ℓ is the path length through the solution. Extinction is caused by light either being scattered or lost to true absorption, where the energy is converted to another form. Microspectrophotometry relies on Beer's law, but applies to images of microscale objects to calculate the absorber's concentration within that object.

2.2.1: Derivation of the Equation to Calculate MCH in COM Images

The following derivation of the relationship between MCH and Beer's law depends on the following simplifying assumptions:

1) The cell in question causes no reflection, refraction, or scattering.
2) Only one Hb form is present, meaning ϵ is known.
3) There is uniform [Hb] concentration inside the RBC and negligible [Hb] outside the RBC.
4) Within a given pixel, the RBC thickness, ℓ, is uniform.

The validity of these assumptions is addressed below in section 2.2.6.

For each pixel covered by an RBC, the following two equations are defined:

$$\mathrm{C} = [\mathrm{Hb}] = \frac{\mathrm{Hb}_p}{\mathrm{V}} \tag{4}$$

$$\mathrm{V} = d^2 * \ell \tag{5}$$

where Hb_p is the number of moles of Hb in the column above the pixel, V is the volume of the RBC portion directly above the pixel, and d is the pixel side-length. The 2nd equation assumes that ℓ is constant over the entire pixel. These two definitions are substituted into Beer's law to yield:

$$\frac{\mathrm{I}_p}{\mathrm{I}_{0,p}} = 10^{\left(-\epsilon\left(\frac{\mathrm{Hb}_p}{d^2\,\ell}\right)\ell\right)} \tag{6}$$

where I_p is the measured intensity of the pixel and $\mathrm{I}_{0,\mathrm{p}}$ is the estimated background intensity, i.e., the intensity expected if no RBC was present. The above equation is not sensitive to ℓ, which is useful because pathlength is not known. The [Hb] term has also been eliminated, which too is not directly measureable in a COM image. Equation (6) is rearranged, yielding

$$\log\frac{\mathrm{I_p}}{\mathrm{I}_{0,p}} = -\epsilon\frac{\mathrm{Hb}_p}{d^2} \tag{7}$$

Converting moles of Hb to mass of Hb via a simple unit conversion, $\mathrm{m}_{\mathrm{Hb},p} = \mathrm{M}_{\mathrm{Hb}} * \mathrm{Hb}_p$, where M_{Hb} is the molar mass, and solving for $\mathrm{m}_{\mathrm{Hb},p}$ yields the mass of Hb above the pixel.

$$\mathrm{m}_{\mathrm{Hb},p} = \frac{\mathrm{M}_{\mathrm{Hb}}\,d^2}{\epsilon}\log\left(\frac{\mathrm{I}_{0,p}}{\mathrm{I}_p}\right) \tag{8}$$

This is summed over all the pixels in the RBC, yielding

$$\mathrm{m}_{\mathrm{Hb,RBC}} = \sum_{p=1}^{\mathrm{P}}\frac{\mathrm{M}_{\mathrm{Hb}}\,d^2}{\epsilon}\log\left(\frac{\mathrm{I}_{0,p}}{\mathrm{I}_p}\right) \tag{9}$$

where P is the total number of pixels covered by the RBC. Once $m_{Hb,RBC}$ is calculated for N RBCs in the image, the MCH is calculated as follows:

$$MCH = \frac{M_{Hb}\, d^2}{N\, \epsilon} \sum_{n=1}^{N} \sum_{p=1}^{P_n} \log\left(\frac{I_{0,np}}{I_{np}}\right) \tag{10}$$

In the MCH equation above, M_{Hb}, d, and ϵ are known constants. I_{np}, $I_{0,np}$, P_n, and N and are outputs from the computer-vision algorithm described in Chapter 3.

2.2.2: Selecting the Illumination Wavelength

To increase the signal-to-noise ratio of the intensity measurements, it is preferable to illuminate Hb at a wavelength where its extinction coefficient is as high as possible. This gives maximum separation of I and I_0, maximizing signal. The absorbance maxima for different forms of Hb occur in the violet region of the visible spectrum (400-430 nm).

As seen in Figure 2, different varieties of Hb have different extinction profiles and maxima. Oxygenated hemoglobin (oxy-Hb) and deoxygenated hemoglobin (deoxy-Hb) both exist in blood, meaning the MCH calculation could depend on their ratio, which would be undesirable. The blood oxygenation of Hb, i.e., the percentage of Hb in oxy-Hb form, varies within the human body from 60% (venous blood) to ~100% (arterial blood)[31]. The vast majority of non-oxygentated Hb exists in deoxy-Hb form, except in cases of blood poisoning. The MCH_{COM} could depend on the oxygenation percentage and thus differ from the true MCH.

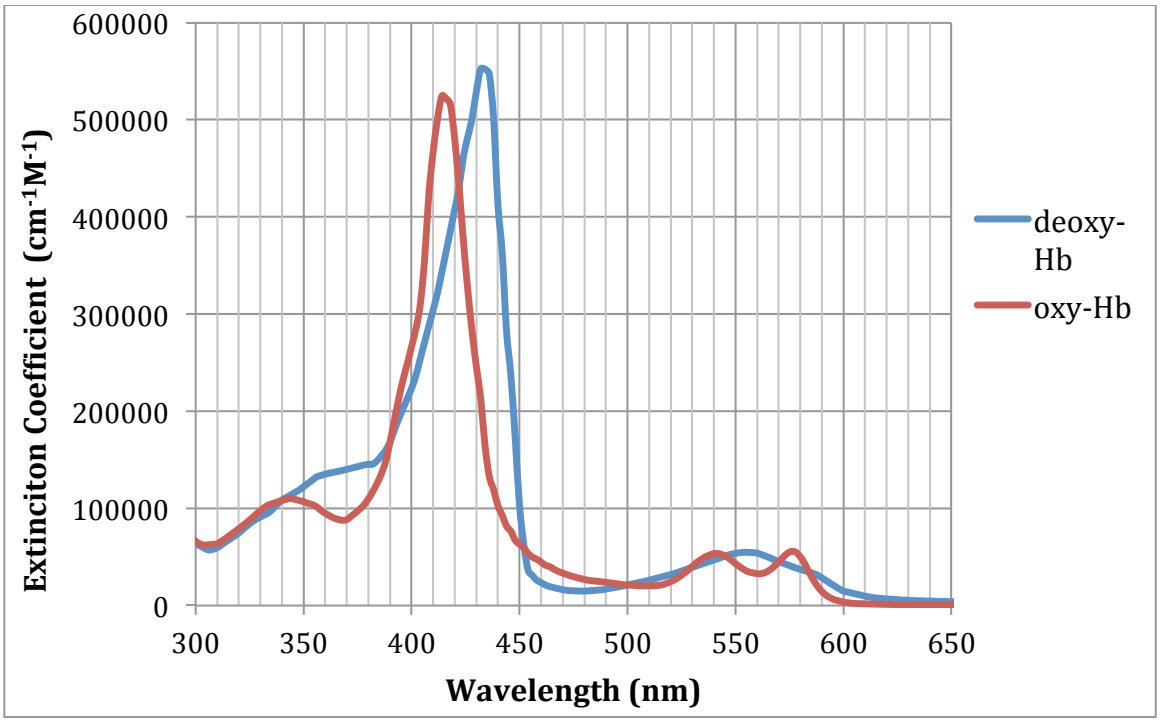

Figure 2: Oxy-Hb and deoxy-Hb absorption spectra [32]

Though oxy- and deoxy-Hb have different extinction profiles, it was suspected that in a real POC test, the vast majority of the Hb would be oxygenated while the blood droplet was still on the subject's finger. If it is assumed that Hb is fully oxygenated, then ϵ_{oxy-Hb} has a maximum value of 5.243 *10^5 $cm^{-1}M^{-1}$, occurring at 415 nm. Substituting this value into Equation (10), as well as M_{Hb} = 64 500 g/mol [32] and d = 1.1 µm (back-illuminated COM pixels have an active area of nearly 100%[33]) yields:

$$\mathrm{MCH} = \frac{1.49}{\mathrm{N}} \sum_{n=1}^{\mathrm{N}} \sum_{p=1}^{P_n} \log\left(\frac{\mathrm{I}_{0,np}}{\mathrm{I}_{np}}\right) \tag{11}$$

Note that the illumination wavelength distribution can alter this coefficient. However, the full width at half maximum (FWHM) of the LEDs used in this research were unknown, though in one case a FWHM of 5 nm was reported in the specification sheet, a value so narrow as to be suspect. The extinction peaks have FWHM of ~20 nm, so if an LED FWHM of 5 nm is assumed, this would decrease the MCH coefficient from 1.49 to 1.44, as calculated by convoluting a Gaussian illumination spectrum centered at 415 nm with the oxy-Hb absorbance profile. With a more likely LED FWHM of 15 nm, this

coeffiecient would decrease further to 1.23, i.e. by 17%. Though significant, this decrease is unlikely to reduce contrast enough to affect measurement precision, as long as the LED wavelength distribution is consistent. Shifting the LED peak wavelength by 5 nm in either direction further decreases the coefficient by only 5%. As a result, the extinction maximum seemed likely to be a reasonable approximation for the net extinction coefficient when calculating the MCH coefficient in Equation 11. In this proof-of-concept research, as long as extinction was dominated by Hb absorbance, the deviation of the MCH coefficient from trueness was of minor importance, for this would simply be integrated into a correction factor relating COM to an StP, as discussed in section 3.7.

Apart from improving the absorbance signal, a second advantage of selecting the extinction maximum is that the signal is less sensitive to small deviations in LED wavelength, since the slope at the peak is 0 (though the drop-off away from the peak is steep, so this effect is limited). A sample COM image obtained using 415 nm illumination is shown in Figure 3.

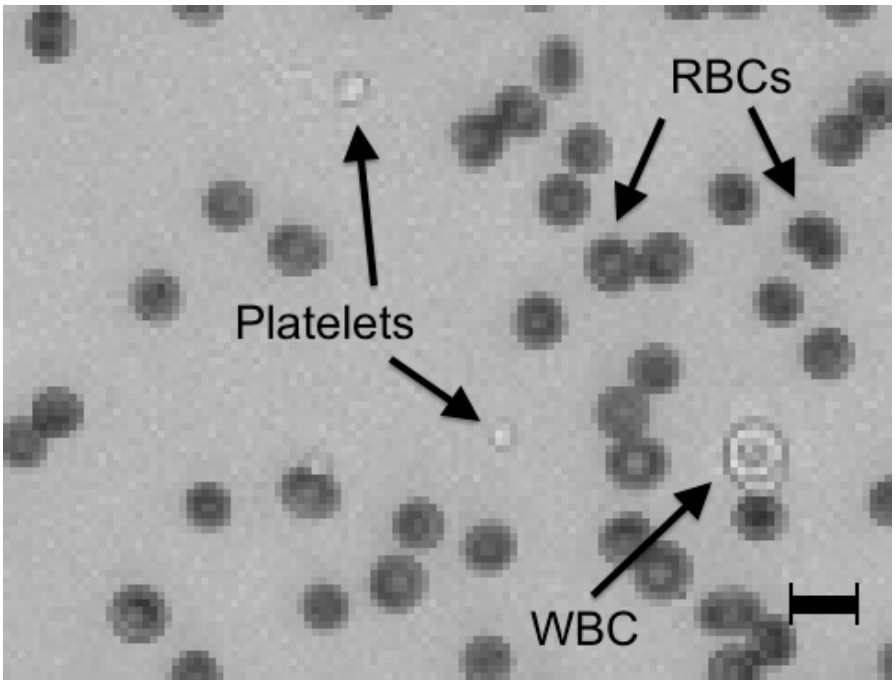

Figure 3: Blood cells in COM using violet (415 nm) illumination. Scale bar shows 10 µm.

As seen in Figure 3, violet illumination resulted in good contrast for RBCs in comparison to platelets and WBCs. Contrast also aids in machine-based RBC segmentation and counting, since RBCs are easily distinguished from other objects in the image.

Note that the error on the extinction profiles was not known, though peak shifts of less than 5 nm do not impact the MCH coefficient substantially. Also, some mutations or pathologies of Hb can lead to significantly different extinction profiles, as in the case of sickle cell anemia, where the peak is shifted to 450 nm[34]. This would typically lead to large miscalculation of the MCH. However, this problem also occurs in StP machines, so physicians are accustomed to diagnosing these conditions by taking other abnormal CBC-parameter values into account[3].

2.2.3: Isosbestic Illumination

It is assumed in the above analysis that all Hb is converted to oxy-Hb. If that is not the case, the MCH correlation is likely to be poor. Pilot data, obtained using the method described above, suggested a poor MCH correlation, and incomplete Hb oxygenation was a plausible explanation. There are different ways to address this potential problem.

One solution is to illuminate the blood at the maximum oxy/deoxy-Hb isosbestic point, 422 nm. Isosbestic points are wavelengths where both forms of Hb have equal absorbance. However, no off-the-shelf LEDs were found at this wavelength. To predict the effect of off-isosbestic illumination, the ratio of measured m_{Hb} to true m_{Hb} can be calculated, where the measured m_{Hb} is calculated under the assumption of full oxygenation. The $m_{Hb,measured}$ is inversely proportional to ϵ_{Hb}, as seen in Equation (8), meaning that the mass measurement of any deoxy Hb will be off by a factor of $\epsilon_{deoxy-Hb}/\epsilon_{oxy-Hb}$, the ratio of true extinction to presumed extinction. To calculate the mass ratio, the mass fractions of oxy-Hb and deoxy-Hb should be added together but with the deoxy-Hb fraction multiplied by the ratio of the extinction coefficients:

$$\frac{m_{Hb,measured}}{m_{Hb,true}} = f + \frac{\epsilon_{deoxy-Hb}}{\epsilon_{oxy-Hb}}(1-f) \tag{12}$$

where *f* is the oxy-Hb fraction, set to 0.6 in the worst case. Converting the mass ratio to a percent difference is straightforward, and the result was obtained that if the illumination is even 1 nm off the isosbestic point in either direction, the resulting Hb mass measurement will off be up to 4%. This is due to the sharply opposing slopes of the oxy/deoxy-Hb absorbance. A wavelength tolerance of <1 nm may be achievable with appropriate illumination sources and optical filters, but a simpler solution was found.

There are other isosbestic points with less severe differences in slopes, such as 390 nm, but these have much lower absorbance, reducing RBC contrast and increasing the impact of scattering and other absorbers, discussed in section 2.2.6. However, this could also be an avenue to pursue.

2.2.4: Conversion to Methemoglobin

Another possibility is to chemically convert both oxy-Hb and deoxy-Hb to a third, single form. StP instruments typically convert all Hb to carboxyhemoglobin (CO-Hb) or methemoglobin (met-Hb) after lysing the RBCs. For Hb microspectrophotometry, Hb needs to be converted within the cell, without damaging the membrane, during a reasonably short incubation time. Fortunately, sodium nitrite ($NaNO_2$) is a suitable conversion agent. Sodium nitrite can pass through the RBC membrane, and it converts both oxy- and deoxy-Hb to met-Hb. Met-Hb is hemoglobin whose iron ions have an oxidation state of 3+, instead of the normal 2+.Oxygen does not bind to met-Hb.

Met-Hb has an absorbance maximum at 405 nm with a 10-20% higher extinction coefficient compared to oxy-Hb[35] (the precise number was not given and had to be estimated from a graph), leading to an MCH coefficient inside the range of 1.19 to 1.34. Assuming the maximum extinction coefficient for met-Hb is 15% higher than that of oxy-Hb, the MCH equation becomes:

$$\mathrm{MCH} = \frac{1.28}{\mathrm{N}} \sum_{n=1}^{\mathrm{N}} \sum_{p=1}^{\mathrm{P}_n} \log\left(\frac{\mathrm{I}_{0,np}}{\mathrm{I}_{np}}\right) \tag{13}$$

Blood and Power [31] showed that conversion of both oxy-Hb and deoxy-Hb to met-Hb in live RBCs is also relatively rapid, particularly when both oxy-Hb and deoxy-Hb

species exist in the blood[31]. Maximum [met-Hb] was reached after 20 minutes with an initial 1:12 nitrite:heme ratio (heme being the oxygen binding subunit of Hb, of which there are four per molecule). The maximum was followed by [met-Hb] decreasing slowly due to methemoglobin reductase activity and reaction with nitric oxide, the byproduct of the conversion of deoxy-Hb to met-Hb[31].

Of potential significance, a side experiment in Blood and Power's study indicated that 10-fold molar-excess nitrite incubated with fully deoxygenated Hb resulted in only 88% met-Hb at equilibrium. Another experiment reported in the literature showed that excess nitrite only converts 50% of pure deoxy-Hb into met-Hb in lysed blood[36]. However, at normal venous blood oxygenation of 60%, the worst-case scenario for capillary blood in normal individuals, ~100% conversion to met-Hb was achieved after 60 seconds (using purified Hb)[36]. Therefore, conversion efficiency and rate is not likely to be an issue, unless there is a major difference in purified Hb or lysed blood compared to whole blood. Though there were no indications in any experiments that this reaction did not go to completion during the four minute incubation time, this posit should be confirmed by dynamic spectroscopy performed on whole blood.

Met-Hb formation is therefore seen as a viable option for improving the reliability of COM-based microspectrophotometry. Using nitrite in large excess is posited to rapidly convert all of the Hb within cells and hold it at the maximum concentration longer than required for a COM experiment.

2.2.5: Statistical Requirements for Number of RBCs Measured

In order to obtain consistently precise estimates of the MCH, it must be ensured that a sufficient number of countable RBCs are present in any COM image. Some RBCs in the images appear in clusters of two or more. These are not included in the MCH calculation due to the difficulty in knowing the number of cells in a cluster. For this research, only isolated, "singlet" RBCs were measured. This reduced the number available for the MCH calculation.

The standard error of the mean of measurements drawn from a Gaussian distribution is

$$e = \sigma/\sqrt{\mathrm{N}} \tag{14}$$

where σ is the standard deviation and N is the number of measurements. Assuming that $m_{Hb,RBC}$ follows a Gaussian distribution between RBCs, this equation can be applied to the MCH measurement, where N is the number of RBCs sampled for the calculation of the MCH. Thus, "$CV_{MCH,sampling}$", the CV of e_{MCH}, is given by:

$$\mathrm{CV_{MCH,sampling}} = \frac{e_{\mathrm{MCH}}}{\mathrm{MCH}} * 100 = \frac{\sigma_{\mathrm{mHb,RBC}}}{\mathrm{MCH}\sqrt{\mathrm{N}}} * 100 = \frac{\mathrm{CV_{mHb,RBC}}}{\sqrt{\mathrm{N}}} \tag{15}$$

where $\sigma_{\mathrm{mHb,RBC}}$ is the standard deviation of the $m_{Hb,RBC}$ measurements (MCH is the mean of these measurements). Solving for N yields:

$$\mathrm{N} = \left(\frac{\mathrm{CV_{mHb,RBC}}}{\mathrm{CV_{MCH,sampling}}}\right)^2 \tag{16}$$

Assuming a worst-case $CV_{mHb,RBC}$ of 50% (this would be highly abnormal clinically), to achieve an ideal value of $CV_{MCH,sampling} < 1\%$, making it essentially negligible with respect to the $CV_{MCH,target}$ of 5%, at least 2000 RBCs need to be sampled, as calculated by substituting these two values into Equation (16).

At roughly 50 pixels per RBC and 8 million pixels in the field-of-view, theoretically over 100 000 RBCs can be packed into the field of view; well over 10 000 RBCs can be packed in while still leaving most of the area as background (which allows for more straightforward calculation of I_0). Based on visual observation of many tests (and as seen in sample images in Chapter 4), the majority of RBCs were singlets, unless the blood was mishandled, which would invalidate the test. Based on observations of StP results from several subjects, the Gaussian assumption was not always completely true, but it was never so severely violated as to call the above analysis into question.

2.2.6: Validity of Microspectrophotometry Assumptions

Beer's law relies on several assumptions that do not necessarily hold true in Hb microspectrophotometry. This can lead to an overall bias, cell-to-cell variation, or person-to-person variation in MCH calculations, the latter because blood from different persons can have different characteristics. Bias is correctable, and the number of RBCs

counted is so large that the error of the estimate of the mean $m_{Hb,RBC}$ will be small, as described above. Person-to-person variation is therefore of the most concern, as this would weaken the correlation between MCH_{COM} and MCH_{StP}.

Variation of Hb Distribution Within a Pixel

An important assumption in Equation (10) is that the product $C\ell$ is constant within a given pixel, i.e., the number of moles of Hb per unit area over every possible subregion of the pixel is identical. This begs the question of how the MCH measurement is affected if the assumption is not valid, and the product $C\ell$ varies within the pixel.

Hypothetically, within the volume above a pixel, if the Hb is all collected in a single tiny column within a pixel, leaving virtually all of the pixel bare, then the measured I_p would be $\sim I_{0,p}$ and measured $m_{Hb,p}$ would be ~0. In mathematical terms, based on Equation (8), if a sub-region above the pixel contains all the Hb, the limit of I_p as the area of this sub-region approaches 0 is $I_{0,p}$, and therefore the limit of the measured $m_{Hb,p}$ is 0. This implies that the more uniform the lateral Hb distribution within a pixel, the more light will be absorbed by the Hb and the higher the measured $m_{Hb,p}$ will be. In the case of uniform lateral Hb distribution, the calculated $m_{Hb,p}$ is maximized and also happens to be correct. Because [Hb] is fairly constant within an RBC[37], variation of ℓ within a pixel will lead to underestimation of $m_{Hb,p}$.

To estimate the impact of this effect on the $m_{Hb,RBC}$ measurement, an extreme case of within-pixel $C\ell$ variation is modeled, where one half of a pixel with uniform Hb distribution has all of its Hb stacked uniformly onto the other half. This roughly approximates what may occur at the edge of an RBC that only covers half a pixel. The true mass of Hb in the pixel is

$$m^*_{Hb,p} = M_{Hb} d^2 C\ell \tag{17}$$

where ℓ is the original, constant height of the volume in question before the Hb restacking. The predicted absorbance, I_p, of this pixel is the linear mean absorbance of both the empty (height of 0) and stacked (height of 2ℓ) halves of the pixel:

$$I_p = \frac{I_{0,p} + I_{0,p} * 10^{-\epsilon C(2\ell)}}{2} \tag{18}$$

To determine the ratio of measured mass to true mass in the pixel, the above is substituted into Equation (8) to obtain the measured mass, and the result is divided by Equation (17), the true mass, yielding

$$\frac{m_{Hb,p}}{m^*_{Hb,p}} = \frac{1}{\epsilon C \ell} \log\left(\frac{2}{1 + 10^{-2\epsilon C \ell}}\right) \tag{19}$$

Met-Hb's estimated absorbance at 405 nm is $6.022*10^6$ $cm^{-1}M^{-1}$ [35], a typical C corresponds to a typical MCHC of 330 g/L [3] divided by the M_{Hb} of 64500 g/mol, and the typical maximum thickness of an RBC is 2.6 μm, half of which is ℓ = 1.3 μm. Substituting the above into Equation (19) yields a ratio of 0.59. This indicates that at the edge of an RBC, the COM-measured m_{Hb} could significantly underestimate the true m_{Hb}. Since edge pixels typically comprise ~1/3 of an RBC's pixels, this has the potential to significantly bias the RBC measurement.

The above effect could also occur in the inner pixels of an RBC, due to the biconcave shape. A typical ratio of the maximum thickness of an RBC to the thickness at the center is 2.6 μm / 1.1 μm = 2.4. In the extreme case where half of a pixel has an ℓ of 1.1 μm and the other half has an ℓ of 2.6 μm, a similar calculation to the above can be performed, resulting in a measured $m_{Hb,p}/m^*_{Hb,p}$ of 0.90. This suggests that variation in thickness within an RBC can also have a significant effect, though not as large as the effect at the edges.

These calculations suggest that the extent to which the $m_{Hb,RBC}$ is underestimated by this effect could vary from cell to cell and person to person with variations in RBC shape. Within a single COM test, or between tests on the same person's blood, the variation of these effects is likely to be negated by the large number of RBCs counted; the bias can be removed by a correction factor. However, these effects may vary from person-to-person depending on a person's natural RBC shape and size. The extent to which this variation will occur is difficult to predict without explicit parametric modeling of cell-to-cell and person-to-person RBC-shape variation, an in-depth simulation task beyond the scope of

this research. The extreme cases calculated above, though, may nevertheless be helpful in interpreting results of MCH_{COM} measurements.

Scattering, Reflection, and Refraction

Beer's law assumes that the detected light does not include any of the scattered light; however, Hb molecules are large enough to scatter some light via Rayleigh scattering. The fraction of total extinction caused by Rayleigh scattering can be calculated. For this calculation, the extinction coefficient of met-Hb at 405 nm is rewritten as an extinction cross-section, $\alpha_{\text{total}} = 9.98 * 10^{-20}\ \text{m}^2$. The scattering cross-section for Rayleigh scattering is given by the equation[38]

$$\alpha_{\text{scattering}} = \frac{2\pi^5}{3} * \frac{z^6}{\lambda^4} * \left(\frac{r^2 - 1}{r^2 + 2}\right) = 4.41 * 10^{-25}\ \text{m}^2 \tag{20}$$

where z is the hydrodynamic diameter of Hb (6.36 nm [39]), λ is the illumination wavelength (405 nm), and *r* is the ratio of Hb's and water's refractive indices. Here, *r* = 1.40 / 1.34 = 1.053 [37]. This leads to $\alpha_{\text{scattering}}/\alpha_{\text{total}} = 4.4 * 10^{-6}$, meaning molecular Rayleigh scattering is negligible and can be ignored.

As stated above, the refractive index of RBCs is higher than the diluted serum, causing light to reflect and refract at the cell membrane. Refraction alters ℓ, the distance light travels through the RBC's body. Incident light will also reflect both when entering and exiting the RBC.

It is not straightforward to estimate the magnitude of these effects, however, due to the fact that the ℓ values for RBCs are on the order of magnitude of the illumination wavelength. For objects at this size scale, light transmission can vary strongly with small changes in size or curvature due to interference effects[40]. In future research, Mie light scattering theory could be used to create a general model for light transmission through RBCs in a COM image[41]. Such a model could potentially allow for corrections based on individual RBCs' predicted shapes and positions over the COM pixels. However, it would be undesirable to introduce such complexity to the MCH measurement unless necessary, and such models are beyond the scope of this research.

Free Hb and Other Absorbers

Beer's law also assumes that there are no scattering or absorption events caused by materials in the blood film other than Hb itself. However, material inside or outside the RBC may also scatter or absorb. These events may lead to overestimation of the MCH if the material is above the segmented RBC pixels, and underestimation if it is not. However, the effect is likely small, as Hb has much higher absorbance than any other blood/diluent component at the wavelengths in question [42], [43].

Reference physiological "free" [Hb] (Hb concentration in the plasma) can be up to 5 μM [44], while reference MCHC values exceed 5000 μM [3], three orders of magnitude higher than the image background levels. This means that free plasma is normally negligible in the MCH calculation.

The assumption of negligible [Hb] outside RBCs may be false if significant hemolysis is present. Excess free [Hb] is caused by some hemolytic conditions. Free [Hb] can rise to 10 μM during severe sepsis[45], or 25 μM during a sickle cell anemia crisis[46]. This is still at least two orders of magnitude smaller than the bottom of the MCHC reference, so it is still negligible.

Another possible source of higher free [Hb] is if hemolysis is induced during sample handling. If a large fraction of the RBCs lyse this could lead to non-negligible free [Hb]. This phenomenon could potentially be detected in computer vision as "ghosting", i.e., barely visible RBCs or RBCs that fade over time. If enough ghost RBCs are present, this could indicate to the COM user or COM software to throw out the test result and repeat it. In any case, a significant degree of lysis is unacceptable for the COM procedure as it may also throw off the measured [RBC].

2.3: Implications

Though the assumptions required for Beer's law fail in some cases, it was posited that they will mostly cause a deviation from the true measurement that is fairly consistent between subjects. For the purposes of this research, a simple linear correlation between MCH_{COM} and MCH_{StP} was hypothesized, of the form $y = ax + b$, where y is the

MCH_{COM}, x is the MCH_{StP} measurement, and a and b are model coefficients. If validated, this model could be used as a correction factor to enable accurate MCH measurement using COM. If there is person-to-person variation, this should appear in data comparing the COM device to the StP as a measureable "random effect", discussed further in the statistical methods section in Chapter 3.

Showing strong correlation of the MCH_{COM} with MCH_{StP} would demonstrate the efficacy of COM-based microspectrophotometry for Hb measurement, and would imply the potential for COM to be used in other microspectrophotometry applications. Such an experiment requires comparison of COM-measured blood sample to StP-measured blood samples from multiple human subjects in order to obtain a range of MCH values corresponding to the required range defined in Chapter 1.

The first such experiment in this research (Experiment 1) involved conversion of all oxy-Hb and deoxy-Hb to met-Hb using $NaNO_2$ in the diluent and 405 nm illumination. A smaller experiment (Experiment 2) retested a subset of the subjects from Experiment 1 using no $NaNO_2$ and 415 nm illumination, on the assumption that all deoxy-Hb was converted to oxy-Hb. The results of the tests using $NaNO_2$ were compared to the results on the same subjects when excluding it. If the system demonstrated poorer performance without $NaNO_2$, it would indicate that met-Hb conversion is crucial to the system, likely due to a varying Hb oxygenation ratio.

Chapter 3: Methods

3.1: Overview

The general method for measuring the MCH on a drop blood using COM is as follows:

1) A drop of blood is mixed and incubated briefly with an appropriate diluent.
2) The blood mixture is injected into the specimen chamber, forming a thin film between the COM sensor and a transparent chamber lid.
3) Multiple images are acquired while light of a specific wavelength is transmitted through the chamber lid to illuminate the cells.
4) The images are processed and analyzed by a computer-vision algorithm to extract the MCH.
5) The specimen chamber is cleaned.

To test the central hypothesis, several blood samples from different individuals were tested on both a single COM device and an StP machine. The data were compared using regression analysis to determine suitable correlation parameters, the coefficient of determination (R^2), and the CV of the residuals.

It should be noted that although measuring MCH is the focus of this research, this measurement ultimately must be obtainable within the context of a procedure that could measure all of the CBC parameters. To that end, the data collection for the research experiments was performed in a manner potentially compatible with the other blood measurements, as discussed in section 1.3.3.

3.2: Diluent

Two diluents were prepared for the experiments, to be mixed with blood at a 3:1 diluent:blood ratio. With the exception of the $NaNO_2$ component, the diluents were designed by other members of Fine's lab. Diluent N, which included $NaNO_2$, contained the following components dissolved in distilled water:

1) 112.3 mM $NaNO_2$

2) 6.5 mM Brilliant Cresyl Blue stain (1% w/w, Sigma, 860867)
3) 21.3 mM Disodium dihydrate EDTA (EM Science, EX0539-1)
4) 5.87 mM HEPES (Sigma, H4034)
5) 5.57 mM KCl
6) 7.36 mM NaCl

Diluent xN, which excluded $NaNO_2$, contained the following components dissolved in distilled water:

1) 6.5 mM Brilliant Cresyl Blue stain (1% w/w)
2) 21.3 mM Disodium dihydrate EDTA
3) 5.87 mM HEPES
4) 5.57 mM KCl
5) 118.6 mM NaCl

The key component of Diluent N diluent was $NaNO_2$, used to convert oxy-Hb and deoxy-Hb to met-Hb. Diluents N and xN were identical except for the replacement in Diluent xN of $NaNO_2$ with a molar equivalent of NaCl. The Brilliant Cresyl Blue stain was included for experiments that are beyond the scope of this research. The diluent was designed to fulfill several functions to ensure that the cells maintained their health and form:

1) Isotonicity, to maintain cell shape and health, was achieved using appropriate concentrations of NaCl, KCl, and $NaNO_2$ in the diluents. The molarity of K^+ mimicked that of blood in order to prevent unwanted changes in membrane potential, which can also change the shape of RBCs[47].
2) Anticoagulation prevents blood cells from aggregating irreversibly, which makes counting them difficult. Ethylenediaminetetraacetic acid (EDTA) was included as an anticoagulant. This is a standard blood anticoagulant that functions by sequestering Ca^{2+} ions [48].
3) The diluent was buffered at physiological pH (~7.4) to maintain cell health[47]. This was accomplished using the HEPES buffer. After preparation of the diluent,

its pH was adjusted to ~7.4 by iteratively pipetting in no more than 5 small drops of highly concentrated HCl or NaOH (5 or 1 M as required for gross or fine adjustments respectively) and measuring the pH using a calibrated Accumet AB250 pH meter. The total volume of fluid added was less than 0.5% of the total volume.

After preparing and pH-balancing the diluents, they were used to dilute a small blood sample at a 3:1 diluent:blood ratio. A thin film of this mixture was then formed by placing a drop between a glass slide and a glass coverslip. This film was examined using transmission microscopy to ensure that the cells were not damaged by the diluent. Cells using diluents N and xN appeared very similar to cells in blood diluted using other formulations that met the requirements described above. In an acceptable diluent formulation, RBCs appear quite circular, with few having bulges or wrinkles. Also, almost all RBCs have light centers surrounded by a darker band. This indicates biconcavity, since the thinner cell center absorbs less light. Further, lack of coagulation is indicated by the individual cells appearing fairly evenly distributed and without stacking.

3.3 Apparatus

3.3.1: COM Sensor

The COM sensor used for this research was an Omnivision OV8850, with 1.1 μm square pixels. The OV8850 contains an array of 3264 x 2448 pixels (~8 million total), with active-area dimensions of 3.6 x 2.7 mm for a field of view of 9.7 mm^2, much larger than a standard microscope's field of view at similar resolution.

The OV8850, as received from Omnivision, had various layers deposited on top of the actual CMOS devices. These are required for standard photography, but hinder COM. The layers were known to include at least microlenses and Bayer-filters. Reactive-ion etching was performed by lab personnel to remove these layers. After etching, the sensor chips were wirebonded by a commercial contractor to printed circuit boards designed by lab personnel. The sensor's wirebonds were then encapsulated for protection, making

sure to leave the sensing region of the chip and some of the surrounding area bare, for a total exposed region of 4.2 x 5.6 mm. The printed circuit board was fixed in position such that the sensor faced directly upward. It was plugged into an Omnivision Redboard interface board, which was connected via USB 2.0 to a Toshiba TECRA R700 computer for sensor control and data acquisition. Images were captured from the sensor using Omnivision's OVTAPanther (version M, 2011/09/08) software, which was also used to set exposure, gain, and video frame rate for the sensor.

3.3.2: Sensor Calibration

The black level of the OV8850 is an "image" of the response of the sensor pixels in absolute darkness. Non-zero values have two components: bias, which does not vary with exposure, and dark current, which is a thermal effect that, theoretically, increases from zero linearly with exposure duration. Beer's law relies on linear relative measurements of I and I_0, but the bias and dark-current perturb the linearity of the sensor. Both bias and dark current components can vary by pixel, so a dark image should be subtracted from all light measurements for the purposes of linearization.

A black-level image of the sensor was obtained by acquiring 20 frames in blackout conditions at 6.00 ms exposure, which were then averaged together to reduce temporal noise. The 6.00 ms exposure was used because all images captured for the MCH experiments used this exposure. When only a single exposure is considered, bias and dark current need not be distinguished. The black-level image's mean pixel value was measured as 2.7 intensity levels out of 256, with a spatial standard deviation of 0.2. This black-level image was subtracted from all experimental images before further processing.

The linear-response of an OV8850 was also characterized. The sensor was illuminated using a 405 nm LED (Mouser Electronics, 749-UV3TZ-405-15) centered 20 cm above the sensor and aimed directly at it, with piece of frosted, microscope-slide glass directly in contact with the LED and parallel to the sensor. The glass acted as a diffusor to flatten the illumination field, though a smooth gradient across the sensor remained, with a maximum difference of 35%. The LED was driven by an Agilent E3648A DC voltage supply set to 15.00 V at full duty cycle, with a 3970 Ω resistor in series. The measured

current was 3 mA. Ten images were captured at 15 different exposures ranging from 0.09 ms to 13.00 ms, such that the whole linear output range was covered. Exposure times were set in the image acquisition software, OVTAPanther. The ten images at each exposure were averaged together, and a black-level "bias" image, captured at 0.00 ms exposure, was subtracted from each averaged image. One thousand pixels were sampled randomly from the result, from the same locations in each image. Simple linear regression was performed on each pixel's output as a function of exposure to determine linearity and offset. As the lighting was not completely flat, some pixels saturated before others. For this reason, the two uppermost exposures were excluded from all regressions.

The mean slope was measured as 21.18 ± 0.04 intensity levels per ms, with a pixel-to-pixel standard deviation of 1.52. The offset was measured as 1.53 ± 0.03 intensity levels with a pixel-to-pixel standard deviation of 1.09. R^2 was measured as 0.9999 ± 0.0001. At the highest exposure included in these regressions, 10.00 ms, the lowest measured intensity out of the 1000 pixels was 200. Thus, the pixels were shown to be highly linear in response up to at least 200 intensity levels, meaning intensity level ratios, as in Beer's law, can be calculated for pixels below 200 intensity levels. (The actual linear upper limit is likely higher.) Assuming a typical background intensity level of 180 and a mean-foreground range of roughly 75-90 (as observed in experimental images), the mean linear offset of 1.53 intensity levels should cause MCH measurements to be underestimated by roughly 1.0-1.3%. Only the variation in this number matters when examining the COM/StP correlation, and 0.3% is negligible compared to the $CV_{MCH,target}$ of 5%.

To characterize temporal noise and local, spatial-gain variation, clusters of pixels were also measured on the dataset acquired above. Two exposures were selected for this analysis: 6.00 ms because this was the exposure used for the MCH experiments, and 10.00 ms because this was near the top of the linear range. From each, 40 five-by-five-pixel squares were selected randomly, using the same squares for all images. These squares were only 5.5x5.5 μm large, so it was assumed that illumination was essentially invariant across them and that any systematic variations were due to gain variations. Temporal noise was measured for each pixel in each square by taking the standard

deviation of the intensity levels across all ten original images (before averaging). The result was mean temporal noise of 2.8 intensity levels for the 6 ms exposure (mean of ~130 intensity levels) and 3.7 intensity levels for the 10 ms exposure (mean of ~220 intensity levels). The spatial standard deviations measured for the squares for the 6.00 ms exposure ranged from 0.5 to 5.2, with a square-to-square mean of 3.2 and a standard deviation of 0.6. In this case the results were virtually identical to the results for the 10 ms exposure.

Theoretically, averaging over 10 images should have reduced the temporal noise level from 2.8 to 0.88 intensity levels for the 6 ms exposure, meaning that most of the spatial variation was likely due to gain variation. Based on typical values of $I = 85$ and $I_0 = 170$ and assuming worst-case total CVs on both of 6%, $\log(I_0/I)$ has a CV of 5%. Measured over 10000 pixels this error is reduced by a factor of 100 to 0.05%. Therefore, measured temporal noise levels and gain variations appear to be too small to impact the MCH measurement.

3.3.3: Chamber Lid

To form the thin blood film on the COM sensor, a transparent chamber lid was required. The material chosen was a flat sheet of 4.5 mm-thick, optically clear, UV-transparent polymethylmethacrylate. A piece of this sheet was CNC-milled into a small block, with a square base of 3.9 x 3.9 mm. The base fit completely within the sensor encapsulation, but covered the entire active sensor area. The base and the upper surface parallel to the base were optically clear so that light could be transmitted through it.

To load the chamber, a drop of blood/diluent mixture was placed on the sensor, and the chamber lid was gently lowered into position set at a height of ~5 μm above the sensor surface. This forced most of the blood mixture out the sides, leaving a thin film of fluid to be imaged.

The chamber height was not measured precisely. However, typical RBCs have a maximum thickness of 2.6 μm, so even if the chamber height varied by 20%, the chamber lid should not squash any RBCs. This height should cause the RBCs to lie flat though, as

they have typical diameters 7.5 μm[49]. When the chamber lid was well seated, RBC stacking was not observed.

3.3.4: Optics

The illuminator for the blood images consisted of two LEDs: a 405 nm LED (Mouser Electronics, 749-UV3TZ-405-15), and a 415nm LED (Lumex, SSL-LXT046UV3C). The LEDs in the illuminator were connected to an Agilent E3648A DC voltage supply set to 15.00 V at full duty cycle. Each LED was placed in series with a potentiometer that was adjusted to bring the average pixel intensity levels to ~190 (as indicated by inspecting many pixel values in real-time via the OVTAPanther display), without approaching LED-current limits. The value 190 was chosen because it was the maximum background value that tended not to saturate any pixels in the image, as observed over several preliminary tests. This also falls within the confirmed linear range of up to 200. Each LED was also placed in series with a manual on/off switch. Resistances and currents were measured with a multimeter (Fluke 77, Series 1) and are found in Table 2. Physically, the LEDs were housed adjacent to each other in an illuminator arm pointing directly downward, with centers ~0.5 cm apart. The illuminator was suspended 20 cm directly above the sensor, allowing the LEDs to act as a quasi-point source (the angle formed by the two LEDs and the center of the sensor was ~1.4º).

Table 2: LED Settings

LED Model	LED Wavelength (nm)	Added Resistance (Ω)	Current (mA)
749-UV3TZ-405-15	405	3970	3
SSL-LXT046UV3C	415	511	23

3.4: Test Protocol

Under a protocol approved by Dalhousie Research Ethics Board, 15 anonymized blood samples and corresponding StP CBCs were obtained from the Victoria General Hospital Hematology lab in Halifax, Nova Scotia. The hematology lab obtained these samples by transferring 1.5-2 mL of blood from the original, EDTA-anticoagulated, venous blood collection tubes into empty 5 mL test tubes, which were then sealed. StP CBCs were then obtained for the contents of each of these test tubes using a Sysmex XN-10

hematology analyzer. This analyzer has $CV_{MCH,precision} < 2.0\%$ for MCH; accuracy was not supplied for MCH, but [RBC] and Hgb, from which MCH is calculated, both have $CV_{MCH,accuracy} < 2\%$. The test tubes were delivered to the Fine lab for COM testing on the same day as the original blood draw. Upon receiving the test tubes, the contents were transferred to 2 mL centrifuge tubes for easier blood handling. The centrifuge tubes were then sealed and kept at room temperature.

To prepare individual tests, 90 µL of diluent was pipetted into sterile 0.5 mL vials, which were then closed to prevent evaporation and kept at room temperature. The standard procedure for performing an MCH test is summarized here and illustrated in **Error! Reference source not found.** First, 30 µL of blood was pipetted from the 2 mL centrifuge tube into a vial containing 90 µl of diluent. This was mixed by inversion and incubated for 4 minutes, at which point 30 µL of blood mixture was withdrawn by pipette and ejected onto the sensor. The chamber lid was lowered onto this droplet to form the blood film. Images were then collected using OVTAPanther image acquisition software, in the order of 4 violet (405 or 415 nm), 4 red, 4 blue, 4 green, and then one more violet for monitoring changes in the cells during the test. (The red, blue, and green-illuminated images were acquired for purposes outside the scope of this research). The time delay between the fluid contacting the sensor and the first acquired image was approximately 13-17 seconds. Images took, on average, just over one second to acquire, and so the time delay between the first and last image was approximately 18-22 seconds. After this acquisition, the chamber lid and the sensor were cleaned. Note that when testing with 415 nm illumination and Diluent xN, the vessels containing blood or blood mixture were left open for as little time as possible to reduce oxygen contamination.

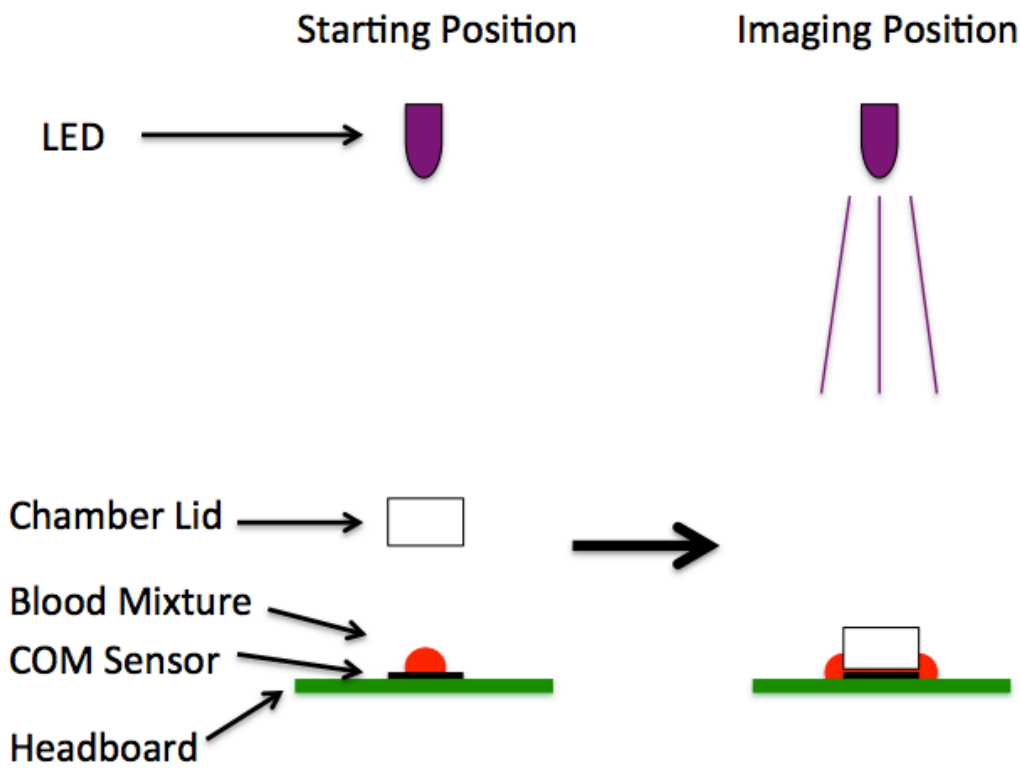

Figure 4: Diagram of testing setup. Left: starting position, with a drop of blood mixture already placed on sensor. Right: the chamber lid is lowered, squeezing out almost all the liquid to form a 5 µm-thick film on the sensor. The LED is turned on, and four images are captured.

3.5: Experiments

Experiment 1: Using Diluent N (nitrite-included) and 405 nm light, blood samples from 15 different individuals were each tested once on the StP. These 15 samples were tested between two and four times each using COM.

Experiment 2: The final six samples used in Experiment 1 were also tested using COM and Diluent xN (nitrite-free) with 415 nm illumination, with between one and four COM tests per sample. For these six samples, the Experiment 2 tests were performed prior to the Experiment 1 tests because the former are likely to be more sensitive to oxygen contamination.

Experiment 3: One of the 2 mL blood tubes was, after testing, left sitting without agitation at room temperature for three days. At this point, the sample was retested with Diluent N. The purpose of this experiment was to explore the possibility that MCH

results are delay-time dependent, as it is possible that RBCs could undergo changes relevant to MCH measurement during the three-day incubation. This issue is further discussed in Chapter 5.

Discards

For Experiments 1 and 2, some tests were discarded. Discards occurred if there was a significant deviation from the standard procedure. Partial shrinkage of many RBCs often became noticeable after less than two minutes of the blood mixture sitting on the sensor (this phenomenon is discussed in Chapter 5). If the blood mixture sat on the sensor for more than ~25 seconds before imaging, compared to the typical 13-17 seconds, the test was discarded, as waiting an extra 10 seconds had the potential to alter the results compared to the normal wait time.

Discards also occurred if there was an obvious problem in the image. For example, a test was discarded if considerable flow of RBCs was observed over the first four images, i.e., if more than 20% of RBCs, as estimated by visual examination of the averaged images, were elongated by a pixel or more in the averaged image. Diffraction artifacts covering more than ~10% of the field of view, as estimated visually, resulted in a discard. These artifacts were typically smooth brightness variations, with peak-to-trough differences of greater than 10 intensity levels and a lateral separation of less than ~100 pixels.

Tests were discarded if the chamber lid or sensor was not adequately cleaned, as indicated by diffraction patterns covering >10% of the image, as estimated by visual examination. Tests were also discarded if a large majority of RBCs appeared in clusters. If a large piece of debris, such as a fiber from a cotton, cleaning swab, was observed in the field of view, the test was discarded. In one case, a test was discarded due to a vast swath of "ghost" (very low contrast) RBCs covering ~10% of the field of view, as this may have indicated Hb leakage (discussed further in Chapter 5).

These discard criteria do not seem likely to be related to the MCH. Furthermore, in an actual POC device, each of these criteria could be recognized by uncomplicated computer-vision algorithms, allowing for an indication to the user that the test should be

discarded. Thus, these discards should not be considered as biasing the results. In a commercial device, the frequency of discards should be minimized, but that was outside the scope of this research.

3.6: Image Processing & Computer Vision

All image processing and computer vision was performed in MATLAB R2012B on a 2011 MacBook Pro running OS 10.9.2 (the "experiment computer"), which contained a 4-core Intel Core i7 processor, 4 GB of random access memory, and 300 GB of storage available on a 5400 rpm hard disk.

3.6.1 Image Processing

The MCH was calculated for each non-discarded test. For the MCH calculations, all images were processed identically. Only the first four violet images were used for the MCH calculation.

These four violet images were averaged together to reduce noise, and the 20-frame averaged 6 ms-exposure darkframe was subtracted, yielding a single master image. The master image was cropped to ~35% of the original size by including only rows 1-1502 (out of 2464) and columns 800-2701 (out of 3280), counting from the top left corner of the image. The included area tended to have fewer illumination artifacts, namely illumination gradients and chamber-lid defects, as seen in Chapter 4. The cropped region, now 1901x1501 pixels, was used by the computer-vision algorithm for the MCH calculation.

3.6.2 Computer Vision

The computer-vision algorithm consisted of three steps:

1) Estimate the background value for every pixel in the image
2) Segment regions containing exactly one RBC (image segmentation)
3) Calculate the MCH using Equation (10)

For step 1, the background level for each pixel in the image was found by shifting a 101x101-pixel window across the whole image by increments of 50 pixels along a single

axis at a time. Because the blood was diluted before imaging, the largest peak in the intensity-level histogram for each window corresponded to background pixels. A Gaussian was fit to this peak using an iterative least-mean-squares function called *gaussfit*, which is freely downloadable[50]. The means of these Gaussians were assigned as the background values at the centers of the windows, and a bilinear interpolation was used to assign background values to the pixels in between the centers of the windows, thus covering the whole image. In each RBC segmentation, the background level calculated for each pixel was assigned to $I_{0,np}$ in Equation (10). RBCs from the outer 50-pixel band were excluded from the MCH calculation as the background values for these RBCs would have to be extrapolated.

This background-estimation method relied on the assumption that large variation in illumination only occurred on scales considerably larger than 50 pixels, which was largely true due to the diffraction-artifact discard criterion. The method also relied on the assumption that fixed-pattern noise and gain variation over lateral ranges smaller than 50 pixels was small in magnitude. This assumption appears to have been supported in section 3.3.2 for ranges of 5 pixels or less. When these assumptions are true, the mean of nearby background-pixel values should be a good estimator for the long-term temporal mean of an unknown background-pixel value.

For the image segmentation of step 2, a COM image was first thresholded with the *greythresh* global-threshold function in MATLAB to produce a binary mask. This function relies on Otsu's method[51]. Otsu's method locates a threshold by maximizing the interclass variance of the foreground and background. RBCs constituted the vast majority of objects passing this threshold, as other cells absorb much less violet light than RBCs. Based on the assumption that the RBCs are roughly circular, or at least convex, an *opening* operation from mathematical morphology, using a 3x3 pixel-structuring element, was performed on the mask. *Opening* consists of two steps: an *erosion* and then a *dilation*. Essentially, the *erosion* shrinks foreground objects by one pixel in all directions, which eliminates objects or projections from objects that are only one- or two-pixels thick. Such objects are not likely to be part of the RBC, since RBCs are roughly

circular. The *dilation* then expands the object so that it once again covers the whole RBC, but, ideally, less of any platelets or small debris adjacent to RBCs that had previously been included in the object.

A size-frequency histogram was then generated for distinct foreground objects in the mask. Thresholded regions diagonally adjacent to others were counted as two separate objects. This histogram typically presented multiple distinct peaks, the largest corresponding to RBC "singlets". Peaks to the left of this singlets peak typically represented platelets or noise, and peaks to the right typically represented clusters of two or more RBCs, as well as occasional, large image artifacts. To measure the MCH, only objects in the singlets peak were desired, to ensure that the value of N from Equation (10), the number of RBCs, had minimal error. To exclude other peaks, a Gaussian was fit to this peak using *gaussfit* to estimate its center, and all objects greater than 1.5x or less than 0.5x the mean of the Gaussian were eliminated. This eliminated the vast majority of noise, artifacts, RBC clusters, and occasional pixels from non-RBC objects. RBC segmentations were also discarded if they contained any pixels with values of 0 or 255, as these are likely to be "hot" or dead pixels, respectively, which could skew the measurement. The remaining objects became the RBC segmentations for the MCH calculation.

Step 3 took the intensity values for the pixels in each RBC segmentation and scanned over them, applying the MCH equations derived in Chapter 2. Equation (13) was used with Diluent N, and Equation (11) was used for Diluent xN.

3.7: Statistical Methods

In order to test the central hypothesis, the MCH values output by computer vision were compared to the StP's "true" values for each test. Statistical analyses were performed in the programming language "R". R version 3.0.2 was used on the experiment computer.

3.7.1: Linear Regression

Regression can be used to model the output of a system based on its input(s), but herein it is used instead to compare two measures of the same phenomenon. Simple linear

regression models data as a straight line with the form $y_i = ax_i + b + \varepsilon_i$, where i indicates the measurement number, x_i are the "perfectly known" measures (MCH_{StP}), y_i are the measures from the new method (MCH_{COM}), and a and b are the coefficients of the model, calculated to minimize ε_i (the residuals). Subsequently, calling a measurement technique "linear" will indicate that it is given by $y = ax + b$, for suitable values of a and b where x is the reference value.

An important assumption for using the model $y_i = ax_i + b + \varepsilon_i$ is that the residuals, ε_i, are drawn independently from a single normal distribution. This assumption fails for these experiments because subjects are resampled up to four times. On top of the "fixed effects" explained by the regression coefficients (a and b) and the random error (ε) introduced by the COM procedure, there is also a "random effect", h, that is caused by factors inherent to the person whose blood was sampled as well as the error of the StP machine. For example, as seen in Chapter 4, several MCH_{COM} measurements for 2 different subjects could have significantly different MCH_{COM} measures despite having nearly identical MCH_{StP} values.

To properly account for this "person" effect (without losing information by simply averaging tests from the same person together), a "mixed-effects" regression model was used for this analysis, of the form

$$y_{ij} = ax_i + b + h_i + \varepsilon_{ij} \tag{21}$$

where i was the subject number, j was the test number for the given subject, h_i was the random effect that varies by subject, and ε_{ij} was the remaining residual error for the particular test. The statistical programming language "R" has a package called *lme4* with a function *lmer* that calculates this model based on the input MCH_{COM} and MCH_{StP} data. The R output gave the regression-model parameters as well as the standard deviations of the random terms (h_i and ε_{ij}). This allowed for determination of COM's sensitivities to different people's blood, distinct from other sources of error.

3.7.2: Correlation & Precision Statistics

The output of the regression contains the parameters *a* and *b* as well as other descriptive statistics, including the coefficient of determination, R^2. R^2, which gives the proportion of the variation in *y* that is explained by the model, can range from 0 to 1, where 1 indicates perfect correlation of the model with the data, and 0 indicates no correlation. In standard linear regression, this value is defined as

$$R^2 = 1 - \frac{\sum {\varepsilon_i}^2}{\sum (y_i - \bar{y})^2} \tag{22}$$

In a mixed model, however, there are two components to the randomness, and it is incorrect simply to lump the random terms together into ε_i. There have been various proposed definitions for R^2 for a mixed-effects model that attempt to convey similar overall information. The definition used herein, developed by Nakagawa & Schielzeth[52], is

$$R^2 = \frac{\sigma_f^2}{\sigma_f^2 + \sigma_h^2 + \sigma_\varepsilon^2} \tag{23}$$

where σ_f^2 is the variance of $ax_i + b$, σ_h^2 is the variance attributable to the random effect, and σ_ε^2 is the variance attributable to random error.

R^2 is a helpful overview statistic, but identical R^2 values cannot be interpreted without further information. This is because intermediate R^2 values could be caused either by random error or a poor choice of model. To analyze this possibility, the residuals ($h_i + \varepsilon_{ij}$) were plotted. Were they to display a noticeable pattern other than random noise, this could indicate a poor choice of model (e.g., a parabola may have been a better fit for the data than a straight line).

For the model used herein, the presence of correlation depends entirely on the statistical significance of the coefficient *a*. Showing that *a* is significantly greater than 0 indicates statistically significant positive correlation between *x* and *y*.

The most important statistic obtained from the model is the total CV for the random terms, $CV_{MCH,total}$, because this estimates the overall $CV_{MCH,precision}$ and can be compared directly to the $CV_{MCH,target}$. This value was obtained by

$$CV_{MCH,total} = \frac{\sqrt{\sigma_h^2 + \sigma_\varepsilon^2}}{a\bar{x} + b} * 100 \quad (24)$$

This value was then compared to the $CV_{MCH,target}$ to determine how well, on average, COM met clinical needs over the range measured. Note that this definition assumes constant variance over the measured range.

To assess the relative contributions to $CV_{MCH,total}$ of h and ε, CVs were also calculated individually for both σ_h and σ_ε. The value of σ_h was calculated via

$$CV_{MCH,h} = \frac{\sigma_h}{a\bar{x} + b} * 100 \quad (25)$$

yielding $CV_{MCH,h}$ and the value of σ_ε was calculated similarly, yielding $CV_{MCH,\varepsilon}$.

3.7.3: Assumptions for Linear Regression

There are other assumptions about the data that must hold for the above model to be valid. These assumptions are described below, and approaches for where the assumptions may not hold are proposed.

Weak Exogeneity

The *x*-variable must have weak exogeneity, i.e., have low enough error relative to the *y*-variable that it (the *x*-variable) can be treated as a true value. The $CV_{MCH,StP}$ used for this research was reported by the manufacturer as "< 2%"[53]. Realistically, the $CV_{MCH,StP}$ is likely much smaller than this given limit, as the StP machine is certified for more extreme values of MCH than are tested in this research.

In the mixed-effects model, the $CV_{MCH,StP}$ presents as a component of $CV_{MCH,h}$, since there is only one StP test per person. The remaining component of $CV_{MCH,h}$ is defined as

$$CV_{MCH,person} = \sqrt{CV_{MCH,h}^2 - CV_{MCH,StP}^2} \quad (26)$$

$CV_{MCH,person}$ is caused by person-to-person variation in MCH_{COM}. If $CV_{MCH,h}$ is greater than ~4%, it is unlikely that the $CV_{MCH,StP}$ had a major impact on the model. This is because when $CV_{MCH,h}$ = 4%, reducing assumed $CV_{MCH,StP}$ from 2% (worst-case) to 0% (best-case) would only decrease $CV_{MCH,person}$ to 3.5%, as calculated from Equation (26). Future studies would benefit either from an explicit characterization of the precision of the StP machine in question or from multiple MCH_{StP} measurements being performed on each blood sample.

Homoscedasticity

Constant variance (homoscedasticity) is another assumption that may not be valid for COM. Linear regression typically assumes that ε has a Gaussian distribution with a constant standard deviation over the measured StP range; however, ε may not be Gaussian if some outlying data points are the result of operator error. If a test meets any of the discard criteria, it should be discarded, but some errors may go unnoticed.

Also, MCH has a theoretical minimum of 0, suggesting that COM's absolute error reduces to zero at extremely low MCH values. This would imply that the error distribution is heteroscedastic. This could interfere with the weighting of the fit if the effect is large enough. However, the measured MCH range for these experiments was relatively small, so this is unlikely to be a serious problem here. It was possible that other forms of heteroscedasticity could occur, such as larger error within a sub-range of the StP values. Heteroscedasticity was checked for by plotting the residuals and looking for variations in σ_ε across the StP values.

3.7.4: Confidence Intervals and Hypothesis Tests

The statistical significance of the model outputs corresponds to the likelihood that individual regression parameters helpfully model the data. R's *lmer* function calculates t-values for the model coefficients, and the *lmerTest* function calculates p-values from these t-values based on Satterthwaite's approximation for denominator degrees of freedom[53]. A p-value indicates the probability that a null hypothesis is true given the data. Here, the null hypotheses are $a = 0$ and $b = 0$. Rejecting the former would show that the MCH_{COM} is a predictor for MCH_{StP}, as implied by the central hypothesis.

Rejecting the later would indicate the need for that term to be included in a correction factor for the MCH_{COM} measurement. The p-values were compared to 0.05, the typical designated confidence level for rejection of the null hypothesis. If a parameter's p-value is lower than 0.05, the corresponding null hypothesis is rejected, and the parameter in question is said to have statistical significance.

The *exactRLRT* function from the *RLRsim* package for R was used to test the significance of *h* in the model. This function uses a bootstrapped restricted likelihood ratio test to compare a model with and without a particular random effect, *h*, to test if inclusion of *h* improves the model, the null hypothesis being that inclusion of *h* makes no difference. This function outputs a p-value that indicates *h*'s significance.

To obtain confidence intervals for $CV_{MCH,total}$ and R^2, a case bootstrap was employed, as suggested by Thai *et al.* for this type of dataset[54]. In this technique, the 15 subjects were resampled randomly, with replacement, to create a new dataset with 15 subjects, with some of the original subjects left out and some repeated. In a case bootstrap, as opposed to other types of mixed-model bootstraps, the tests within each subject are not resampled. This process was repeated 1000 times, and $CV_{MCH,total}$ and R^2 were calculated for each resampling. The values obtained collectively represent an estimation of the distributions of these parameters. These distributions were then used to determine 95% confidence intervals and to test the hypothesis that $CV_{MCH,total} < CV_{MCH,target}$.

3.7.5: Bland-Altman Analysis

Bland-Altman analysis is a standard biostatistics method to determine the equivalence of two techniques for measuring the same parameter[55]. In this method, a plot is constructed where the vertical axis is the mean of two corresponding data points, and the horizontal axis is their difference. However, these experiments were performed to determine if a correlation exists between the MCH_{StP} and the MCH_{COM}, rather than to show their equivalence, which in this case would require $a = 1$, $b = 0$, and $CV_{MCH,total} \sim CV_{MCH,StP}$. This was not expected to be the case; therefore, Bland-Altman analysis was premature. A subsequent experiment using Bland-Altman analysis could be performed after using the regression models obtained in this research as correction factors for new

data. This is the ultimate test required to compare COM's accuracy to the StP's accuracy for CBC measurements.

Chapter 4: Results

4.1: Imaging

4.1.1: Sample Images

The following figures show examples from the collected images. The images shown here are typical of the collected images. Figure 5 shows a full-field sample image from Experiment 1, using Diluent N (nitrite included) and 405 nm illumination.

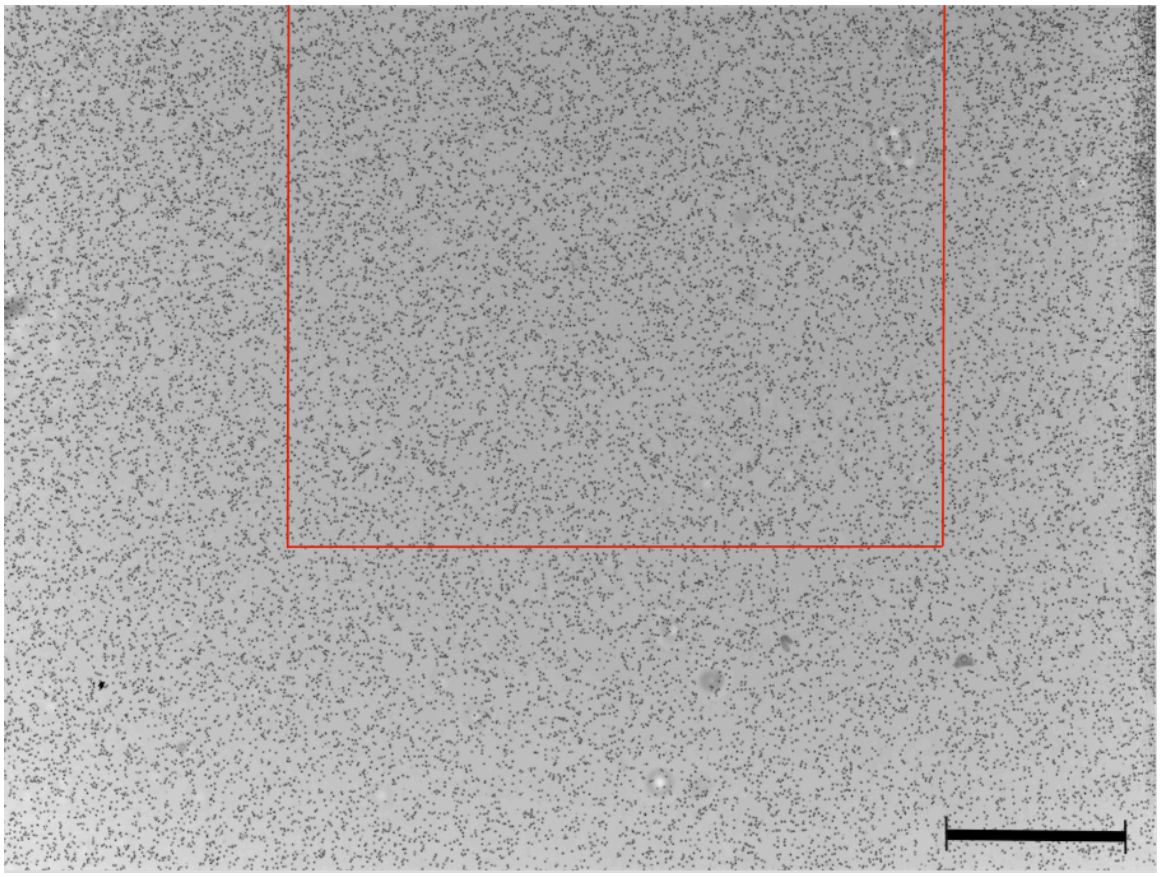

Figure 5: Sample full-field image using 405 nm illumination and Diluent N. The red box indicates the region selected for the MCH calculation. Scale bar indicates 0.5 mm.

Figure 5 demonstrates the appearance of COM images. The illumination was not completely even across the whole image, but was fairly smooth except in specific locations that had defects. In Figure 5, as in all collected images, a shadow cast by the chamber lid's edge could be seen on the right edge of the image. Also, the background was typically 15-25% brighter in the bottom left corner. These artifacts were only

present when blood mixture was loaded into the chamber, and were therefore difficult to correct. By selecting a subregion for the MCH calculation, these artifacts were avoided.

Figure 6 shows a small region from an image obtained using Diluent N.

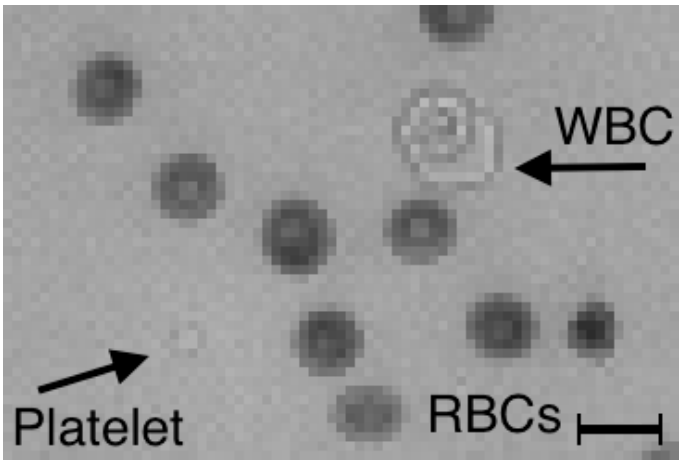

Figure 6: Sample image subregion using 405 nm illumination and Diluent N. Scale bar indicates 10 µm, equivalent to 9.1 pixels.

As seen in Figure 6, RBCs appear visually to have excellent contrast and are clearly distinguishable from WBCs and platelets.

Figure 7 shows a small region from an image obtained using Diluent xN.

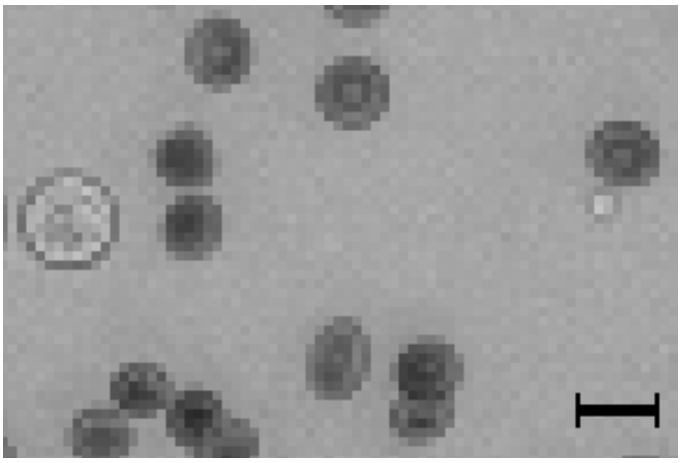

Figure 7: Sample image subregion using 415 nm illumination and Diluent xN. Scale bar indicates 10 µm, equivalent to 9.1 pixels.

The images with Diluent xN were very similar to the images with Diluent N, with RBCs having good contrast and distinguishability from other cell types.

4.1.2: Ghost RBCs

In some tests, a small percentage of the RBCs faded during the 18-22 s imaging sequence, producing "ghost" RBCs. Such RBCs are indicated in Figure 8 (Subject 4, Diluent Y), which shows the first and last frames from the imaging sequence, captured roughly 18-22 seconds apart. In Figure 8, it can be seen that at least two of the three indicated RBCs were already fading before the first image was captured, and were almost invisible by the time the last image was captured.

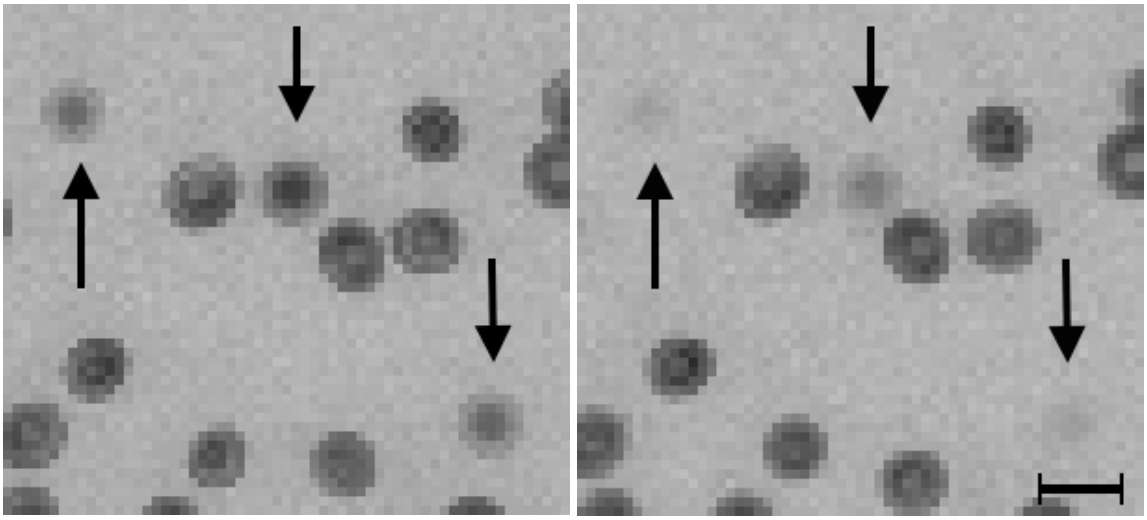

Figure 8: Example of ghost RBCs. Left: first frame from a Subject 4 Diluent N test. Right: final frame. Ghost RBCs are indicated by arrows. Scale bar indicates 10 µm, equivalent to 9.1 pixels.

Ghost frequency varied considerably from subject-to-subject, test-to-test, and region-to-region within an image. To estimate the worst-case scenario for ghost frequency, 300x300-pixel boxes were drawn around four randomly selected ghosts (one from each quadrant of the image) from Subject 4 Test 2, the test in the dataset that appeared to contain the most ghosts. The number of ghosts and intact RBCs were counted in each box. This resulted in 10/269, 2/351, 6/319, and 2/396, in the four boxes, giving 20/1335 = 1.5% in total. Since RBCs occupy roughly 10% of the volume of the diluted blood, the concentration in the fluid outside the RBCs would have increased to 1.5%/10 = 0.15% of the concentration inside RBCs. Thus, in the worst case, even if the true number of ghosts was somewhat underestimated, the impact on the Hb mass measurement was likely negligible.

4.1.3: Discards

Two examples of discarded tests are shown below. Figure 9 shows a test that was discarded due to excessive diffraction artifacts. Presumably this was due to the upper surface of the chamber lid being cleaned improperly, as the effect disappeared after proper cleaning.

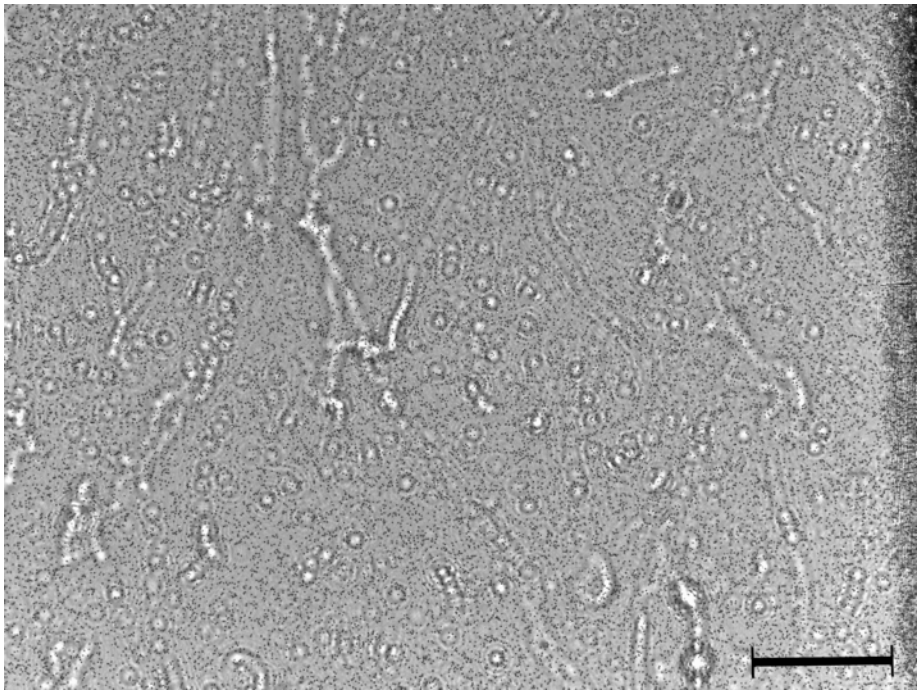

Figure 9: Full-field image from test discarded due to diffraction artifacts. Scale bar indicates 0.5 mm.

Figure 10 shows a test that was discarded due to a fiber in the field of view. Fibers like this, presumably originating from the cotton swabs used to clean the chamber lid and sensor, occasionally appeared in the field of view. These tended to increase the RBC concentration and vary the RBC distribution over field of view, as seen in Figure 10. It is possible that the fiber prevented the chamber lid from being well seated on the 5-μm spacer, resulting in an excessive amount of blood mixture in the chamber.

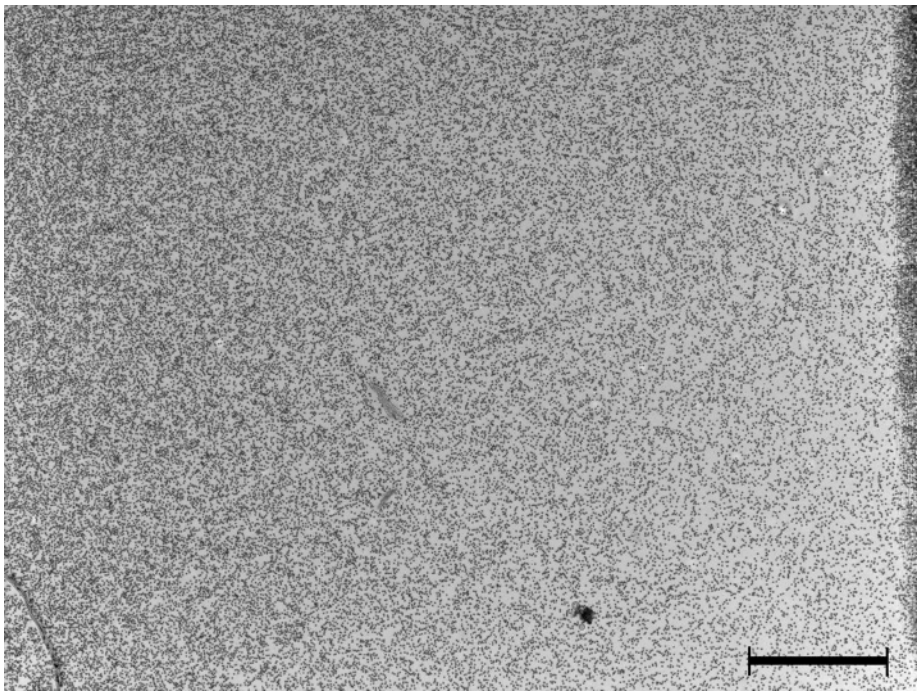

Figure 10: Full-field image from test discarded due to a fiber in bottom left corner and excessive RBC concentration. The black dot near the bottom of the image was also debris. Scale bar indicates 0.5 mm.

4.2: MCH

For the subsequent analyses, relevant information is reported in figures containing pairs of data plots and figures containing R output. In the plots on the left, MCH_{StP} values are plotted on the horizontal axis and MCH_{COM} values are plotted on the vertical axis. The data, the mixed-model regression line, the R^2 value, and the required range are displayed. In the plots on the right, the residuals are shown, as well as lines corresponding to $CV_{MCH,total}$, $CV_{MCH,target}$, and the required range. The corresponding R output is shown in the figure following each pair of plots.

4.2.1: Experiment 1:

The results for Experiment 1 (Diluent N) are shown in Figure 11 and Table 3.

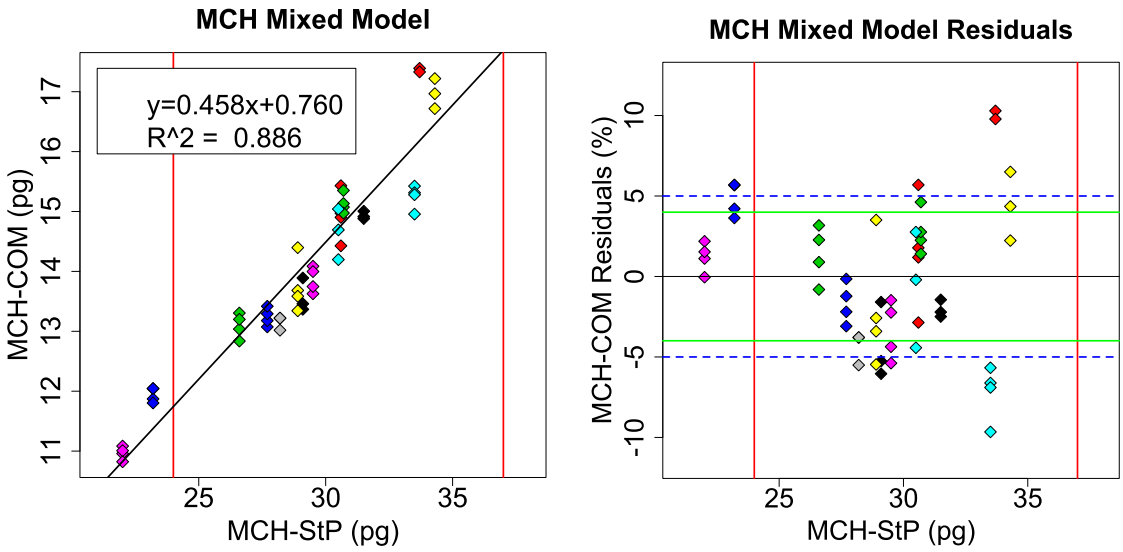

Figure 11: Experiment 1 MCH results. Colour of point marker helps to distinguish the data by subject (some colours are reused, but all subjects have unique MCH_{StP} measurements). Vertical red lines indicate the limits of the required range. Left: data and regression line. Right: residuals plot (solid green horizontal lines: ± $CV_{MCH,total}$; dotted blue horizontal lines: ± $CV_{MCH,target}$)

Table 3: Experiment 1 (Diluent N) R output. 1st section: *lmer* fixed-effects. "df" refers to degrees of freedom. 2nd section: N-values, R^2, CVs, *exactRLRT* p-value, and measured ranges. 95% confidence intervals in square brackets.

	Estimate	Std. Error	df	t-value	p-value
b	0.7596	1.1755	12.57	0.646	0.530
a	0.4576	0.0398	12.61	11.487	$4.8*10^{-8}$

Number of Subjects	15
Number of Tests	53
R^2	0.886 [0.831,0.930]
$CV_{MCH,target}$	5%
$CV_{MCH,total}$	3.99% [3.81,4.19]
$CV_{MCH,h}$	3.57%
$CV_{MCH,\varepsilon}$	1.78%
exactRLRT p value	0
Measured Range	22-34.3 pg
Required Range	24-37 pg
% of Required Range Measured	79%

As seen in Figure 11, there was a strong linear correlation between the MCH_{COM} and the MCH_{StP}. The model has an *a* of 0.46 ± 0.04, indicating a positive correlation, with a near-zero p-value, indicating that *a* is significantly different from 0 and that therefore that the correlation is statistically significant. R^2 is calculated as 0.89 with a 95% confidence interval of [0.83, 0.93], which also indicates strong correlation. The model has a *b* of 0.76 ± 1.2 with p approximately 0.5, indicating that *b* is not significantly different from 0.

The $CV_{MCH,total}$ was calculated as 3.99%, with a 95% confidence interval of [3.81, 4.15]. This is significantly smaller than the $CV_{MCH,target}$ of 5% with high confidence, meaning it appears that COM meets the precision requirement established in Chapter 1.

The $CV_{MCH,h}$, measured at 3.57%, represents the variation caused by the random effect. With an *exactRLRT* p-value of 0, *h* is shown to be statistically significant (as mentioned in Chapter 4, *exactRLRT* is an R function that tests the significance of a random effect in a mixed regression model). $CV_{MCH,h}$ includes two components: $CV_{MCH,StP}$ and

$CV_{MCH,person}$. At < 2%, $CV_{MCH,StP}$ is likely a minor contributor to $CV_{MCH,h}$. In the worst case that $CV_{MCH,StP}$ = 2%, $CV_{MCH,person}$ would be 2.95% as calculated from Equation (26).

$CV_{MCH,\varepsilon}$, measured at 1.77%, represents the other sources of error in the COM measurement. With MCH_{COM} measurements ranging from 10.96 – 17.60 pg, $\sigma_{\mathrm{mHb,RBC}}$ ranging from 2.0 – 3.7 pg, and 3100-6100 RBCs counted per image, $CV_{MCH,sampling}$ was calculated from Equation (15) to range from 0.17% to 0.37 % over the 53 tests. This indicates that $CV_{MCH,sampling}$ was a negligible contributor to $CV_{MCH,\varepsilon}$. Overall, $CV_{MCH,person}$ appears to be the most important contributor to $CV_{MCH,total}$.

The measurements covered 79% of the required MCH_{StP} range, as well as a small region below the required range, but missed the upper 21% of the required range. Coverage was sparse around the MCH_{StP} values of 25 pg and 32 pg. Observing the residuals plot in Figure 11, there appears to be noticeable heteroscetasticity, with a larger $CV_{MCH,h}$ toward the upper end of the range, though $CV_{MCH,\varepsilon}$ appears to be relatively constant.

4.2.2: Experiment 2:

Figure 12 and Table 4 show the results for Experiment 2 for tests performed using 415 nm illumination and no nitrite (Diluent xN).

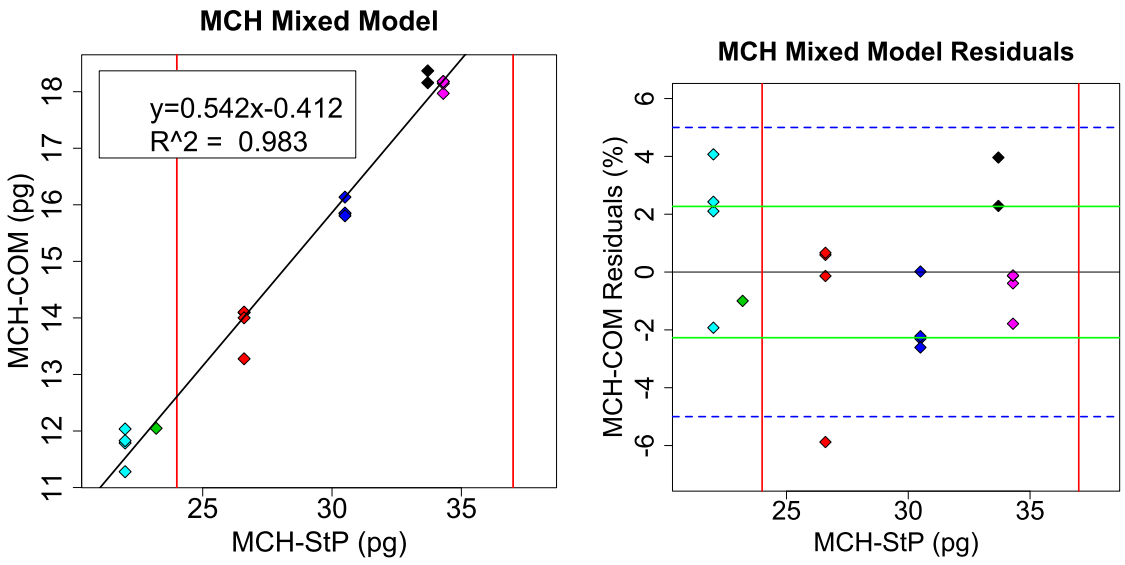

Figure 12: Experiment 2 MCH Results (Diluent xN). Colour of point marker distinguishes the data by subject. Vertical red lines indicate the limits of the required range. Left: data and model. Right: residuals plot (solid green horizontal lines: ± $CV_{MCH,total}$; dotted blue horizontal lines: ± $CV_{MCH,target}$)

Table 4: Experiment 1 (Diluent xN) R output. 1st section: *lmer* fixed-effects. "df" refers to degrees of freedom. 2nd section: N-values, R^2, CVs, *exactRLRT* p-value, and measured ranges.

	Estimate	Std. Error	df	t-value	p-value
b	-0.4117	0.6675	3.81	-0.617	0.572
a	0.5425	0.0230	3.77	23.57	$3.15*10^{-5}$

Number of Subjects	6
Number of Tests	19
R^2	0.983
$CV_{MCH,target}$	5%
$CV_{MCH,total}$	2.27%
$CV_{MCH,h}$	1.43%
$CV_{MCH,\varepsilon}$	1.75%
exactRLRT p value	0.062
Measured Range	22-34.3 pg
Required Range	24-37 pg
% of Required Range Measured	79%

To best compare Diluent xN with Diluent N, the Experiment 1 (Diluent N) data for only the six subjects also tested with Diluent xN were used in the comparison. The Diluent N data for these subjects are shown in Figure 13 and Table 5, with a mixed-model recalculated for just these subjects.

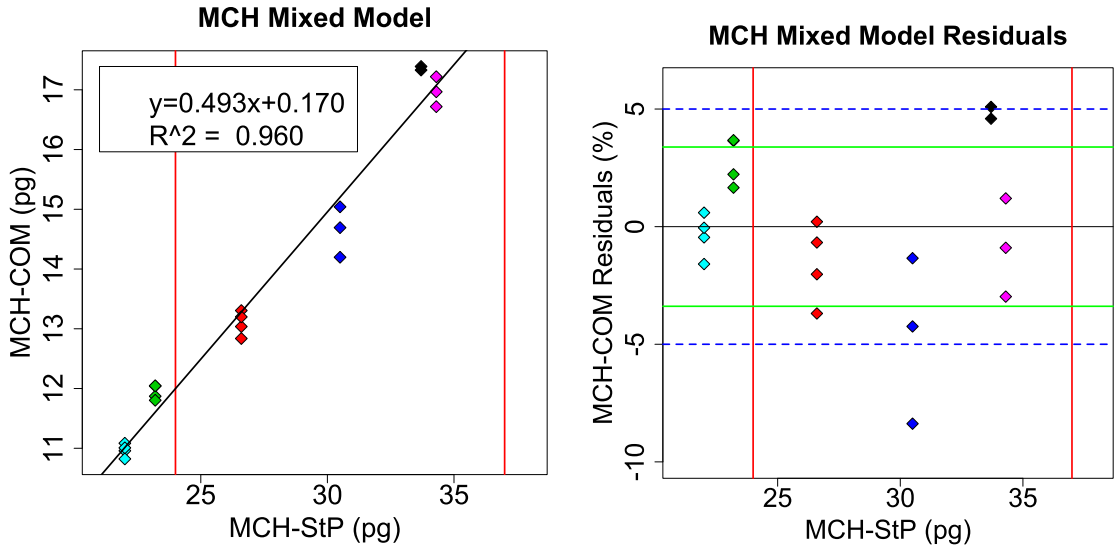

Figure 13: Experiment 2 MCH Results (Diluent N). Colour of point marker distinguishes the data by subject. Vertical red lines indicate the limits of the required range. Left: data and model. Right: residuals plot (solid green horizontal lines: ± $CV_{MCH,total}$; dotted blue horizontal lines: ± $CV_{MCH,target}$)

Table 5: Experiment 2 (Diluent N) R output. 1st section: *lmer* fixed-effects. "df" refers to degrees of freedom. 2nd section: N-values, R^2, CVs, *exactRLRT* p-value, and measured ranges.

	Estimate	Std. Error	df	t-value	p-value
b	0.1698	1.0799	3.84	0.1573	0.883
a	0.4929	0.0376	3.88	13.101	$2.35*10^{-4}$

Number of Subjects	6
Number of Tests	20
R^2	0.960
$CV_{MCH,target}$	5%
$CV_{MCH,total}$	3.38%
$CV_{MCH,h}$	2.99%
$CV_{MCH,\varepsilon}$	1.57%
exactRLRT p value	0.0006
Measured Range	22-34.3 pg
Required Range	24-37 pg
% of Required Range Measured	79%

The results of the Diluent xN tests and the corresponding Diluent N tests were somewhat similar. Both met the $CV_{MCH,target}$ requirement, with similar $CV_{MCH,total}$'s of 2.27% and 3.38% respectively. For these subjects, the correlation was very strong for both Diluent N and xN, with R^2 values of 0.96 and 0.98 respectively, compared to 0.89 for Experiment 1. The confidence intervals could not be bootstrapped due to the small sample size, but the Diluent xN results appear to be somewhat better than the Diluent N results.

In Experiment 2, both Diluents N and xN had considerably better $CV_{MCH,total}$ values and much better R^2 values than Experiment 1. However, since the Experiment 2 subjects are a subset of the Experiment 1 subjects, and the number of subjects is small, this is of questionable importance.

Both tests had similar $CV_{MCH,\varepsilon}$ values, with 1.57% for Diluent N and 1.75% for Diluent xN. The MCH_{StP} range, the $\sigma_{mHb,RBC}$ range, and the RBC count range were found to be similar to Experiment 1 for both diluents, meaning $CV_{MCH,sampling}$ ranged from 0.17-0.37% and was therefore a negligible contributor to $CV_{MCH,\varepsilon}$.

The difference in $CV_{MCH,total}$ between Diluent N and Diluent xN was accounted for by the random effect. The Diluent N tests had a larger $CV_{MCH,h}$ of 2.99% compared to 1.43% for Diluent xN. For both, but especially Diluent xN, $CV_{MCH,StP}$ could have been a significant contributor to $CV_{MCH,h,}$, potentially accounting for all of the variation in the latter. For Diluent xN, *h* is not quite statistically significant, with an *exactRLRT* p-value of 0.062, whereas it is highly significant for Diluent N, with an *exactRLRT* p-value of 0.0006.

Diluent xN has a statistically significantly larger *a*, 0.54 ± 0.2, than Diluent N which had an *a* of 0.49 ± 0.4. Both had *b* values that were statistically indistinguishable from 0. (Comparing the Diluent N subsample here to the full Experiment 1 results, *a* and *b* are insignificantly different.)

The measurements in Experiment 2 are relatively uniformly drawn from the measured StP range, lending confidence to the results. There is no obvious heteroscdasticity for Diluent N or Diluent xN.

4.3: Computer Vision

The computer-vision algorithm took roughly 12-20 seconds per test when run on the experiment computer.

A representative example of the segmentation results and background estimation is shown in Figure 14.

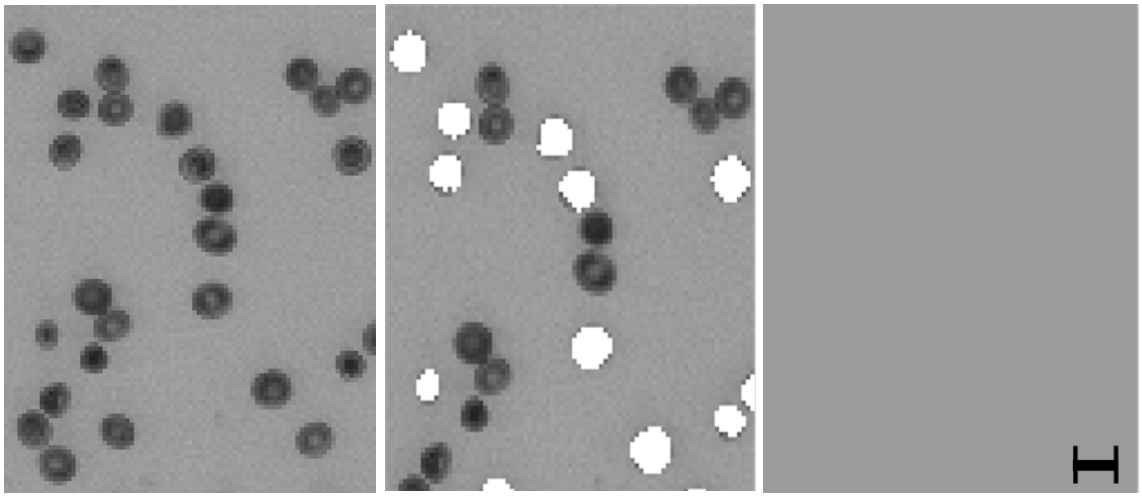

Figure 14: Computer vision results sample. Left: Sample region of an Experiment 1 test (Subject 15, Test 1). Middle: RBC singlet segmentations overlaid in white. Right: background estimation. Scale bar indicates 10 µm, equivalent to 9.1 pixels.

Segmentations and background estimation results were visually similar across all subjects and tests, and did not appear to vary between Diluents N and xN.

Deficiencies in the computer-vision algorithm may have contributed to the values obtained for a, b, h_i , and ε_{ij} , and in turn to R^2, $CV_{MCH,total}$, $CV_{MCH,\varepsilon}$, and $CV_{MCH,h}$. To explore this, the segmentations for all images were scanned visually for errors in the segmentation. Additionally, to obtain rough algorithm-performance estimates, five 200x200-pixel sample frames, each from a different subject, were analyzed in more detail using ImageJ software (version 1.49m)[56]. One of these tests was selected from the low end of the MCH_{StP} range (randomly from Subject 12), one was selected from the middle of the range (randomly from Subject 6), and three were selected from the upper range (randomly from Subjects 5, 10, and 15 – Subjects 5 and 10 were outliers from the regression model).

4.3.1: Background Estimation Assumptions

The background estimation algorithm produced smooth background except in rare windows where the *gaussfit* function did not converge, typically in locations with illumination defects. In each of the five 200x200-pixel frames analyzed, five rectangular-shaped selections of 60-150 background pixels were measured, four from near the corners of the frame and one from near the center. The size and location varied due to RBCs being in different locations in each image. The standard deviation within these selections was never more than 5 intensity levels, and usually less than 4. Mean intensity levels in these selections never differed by more than 5.3 intensity units within a frame. It therefore seems reasonable to infer that the background was sufficiently smooth, fulfilling the assumption required for the background estimation algorithm. With over 3000 RBCs measured in each test and typically over 40 pixels per RBC segmentation, there were likely more than 120 000 individual pixel measurements made in each test, so

minor deviations of the background estimation from trueness were likely averaged out over all these measurements.

4.3.2: False Positives/Negatives

In the five closely analyzed 200x200-pixel frames, no false-negative or false-positive RBC singlets were found out of 288 total singlet RBCs segmented. In the images more generally, there were very few false positives and negatives (with the exception of the Experiment 3 image, discussed in section 4.4), and it seems unlikely that these would have strongly impacted the measurements. On very rare occasion two small, touching RBCs were identified as a singlet. Under diffraction illumination artifacts, which themselves were rare, RBC singlets were often missed. However, these are also the regions where the background estimation was least accurate, so excluding these RBCs from the MCH measurement was likely beneficial.

4.3.3: Extra Pixels

Sometimes extra pixels, belonging to adjacent platelets or debris, were included in RBC segmentations. In the five frames examined, this occurred once on average per frame, out of an average of 70 singlet segmentations per frame. The extra measured m_{Hb} for the RBCs that had extra pixels varied considerably, from 4% to 60%, as compared to the test's overall MCH. Dividing by 70 to account for frequency, the MCH bias due to extra pixels was estimated as 0.06-0.8%, meaning the "$CV_{MCH,extra\text{-}pixels}$", i.e., the variation in MCH_{COM} measurements due to extra pixels, was roughly 0.8% in the worst case. This was not enough to make a large contribution to $CV_{MCH,\varepsilon}$ (1.77%), let alone $CV_{MCH,h}$ (3.57%) or $CV_{MCH,total}$ (3.99%). Based on visual examination of many segmentations, it did not appear that some tests consistently included extra pixels from debris or platelets more often, though this was difficult to judge visually. The sample size used here for estimating $CV_{MCH,extra\text{-}pixels}$ is very small, so it is possible that $CV_{MCH,extra\text{-}pixels}$ was actually somewhat larger than 0.8% and contributed significantly to $CV_{MCH,\varepsilon}$ or even $CV_{MCH,h}$. However, this seems unlikely.

4.3.4: Missed Pixels

The *greythresh* function, which used Otsu's method, followed by the *opening* operation typically resulted in several pixels being missed from the outside edges of most RBC segmentations. This problem appeared to be more serious than the extra-pixels problem and was therefore characterized in more detail. For the same tests as used for the background-smoothness estimation and the extra-pixel estimation (one test each from subjects 5, 6, 10, 12, 15), the following method was used to measure the impact of missed pixels on the MCH_{COM} measurements.

Method

First, 30 RBC-singlet segmentations were selected at random from each of these tests, and an additional *dilation* operation with a 3x3-pixel structuring element was performed on each. This expanded the segmentation by one pixel in all directions to ensure that all pixels in the RBC were included (in the vast majority of cases). Each dilated segmentation was examined visually to check if they included pixels darkened by objects apart from the RBC in question. If this occurred, the RBC was discarded, resulting in 19-24 segmentations remaining per image. For each remaining RBC, Equation (13) was used to calculate $m_{Hb,RBC}$ for both the original segmentation and the dilated segmentation. The difference between these two values was expressed as a percentage of the $m_{Hb,RBC}$ of the dilated segmentation. This represented the percent underestimation of the $m_{Hb,RBC}$ due to pixels missed by the original computer-vision algorithm. The mean of these 19-24 underestimations was found for each test, yielding a percent bias estimate for each test. The test-to-test mean percent bias was taken to estimate the overall bias in the MCH_{COM} measurements caused by missed pixels. Five corresponding standard deviations were found for each test, and the error on each bias value (e_i, where i is the test index) was then calculated using Equation (14).

The biases' CV can be thought of as "$CV_{MCH,missed\text{-}pixels}$", which represents the extent to which missed pixels contributed to $CV_{MCH,total}$. To account for the errors in the percent bias estimates when calculating $CV_{MCH,missed\text{-}pixels}$, a Monte Carlo simulation was used. In this method, a random number was drawn from a Gaussian distribution ($\mu = 0$, $\sigma = e_i$) for

each test and added to that test's percent-bias value. The CV of these perturbed bias values was taken. This was repeated 1000 times, and the mean of these CVs represented $CV_{MCH,missed\text{-}pixels}$.

Results

As determined by visual observation, the *dilate* operation caused pixels to be missed very rarely, compared to 10-14 missed per RBC in the original segmentation. Furthermore, the pixels missed by the original segmentation were not very dark, so the MCH_{COM} biases only ranged from -9.0% to -11.8% (each with standard error $\leq$ 1.0%) for a mean of 10.2%. $CV_{MCH,missed\text{-}pixels}$ was found to be 1.4%. It is not possible from the limited data collected here to separate $CV_{MCH,missed\text{-}pixels}$ into its potential contributions to $CV_{MCH,h}$ and $CV_{MCH,\varepsilon}$. However, it seems that the $CV_{MCH,missed\text{-}pixels}$ of 1.4% could not have made a large contribution to the $CV_{MCH,h}$ of 3.57%. The 1.4% variation is large enough to have contributed significantly to the $CV_{MCH,\varepsilon}$ of 1.77%.

4.4: Experiment 3

The blood sample from Subject 15 was incubated at room temperature for three days and then imaged again on COM, once again using Diluent N. As seen in Figure 15, the RBCs imaged after the incubation were noticeably different from the RBCs in the original tests. In the three-day incubated sample, most RBCs appeared to be smaller, more uniform, and with darker centers.

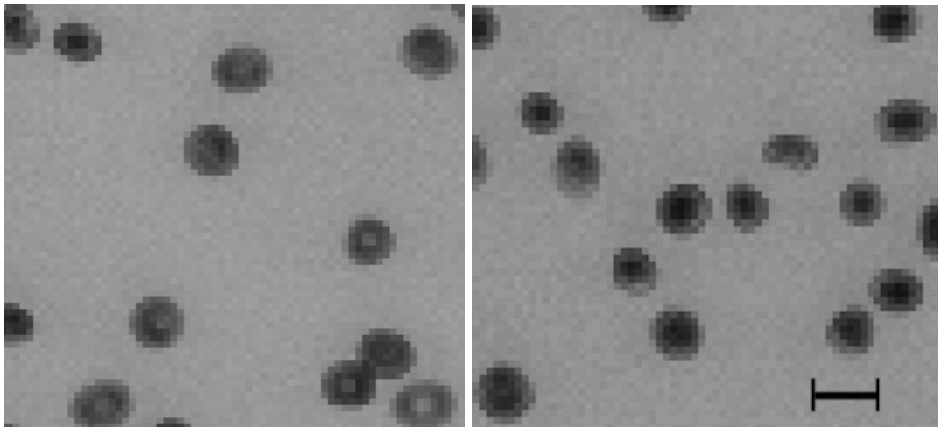

Figure 15: Shrunken RBCs in Experiment 3. Left: Subject 15, same-day test (Diluent N). Right: Subject 15, three-day incubation test (Diluent N). Scale bar indicates 10 µm, equivalent to 9.1 pixels.

The model-corrected MCH_{COM} for the three-day incubated sample was measured as 31.8 pg. The original tests on the same subject had model-corrected MCH_{COM} measurements of 34.9, 35.4, and 36.0 pg for a mean of 35.4 pg and a standard deviation of 0.6 pg. The three-day test's MCH_{COM} measurement was 9.9% smaller than the mean of the same-day tests. This amounts to 6.7 standard deviations, a statistically significant difference.

In the three-day incubation test, the computer-vision algorithm missed some of the largest RBC singlets that had not shrunk, presumably because they were categorized as RBC clusters. In a sample region of the image that comprised 11% of the total area, six missed RBC singlets were counted, giving $e_{\mathrm{count}} = \sqrt{6} = 2.4$. There were 4146 RBC singlets counted in the total area used for the MCH calculation, so it was estimated that the percentage of RBCs missed was

$$\frac{6 \pm 2.4}{0.11} * \frac{100}{4146} = 1.3\% \pm 0.5 \tag{27}$$

These missed RBCs are unlikely to have had a mean $m_{Hb,RBC}$ of more than double the MCH_{COM} value measured for the test. On this assumption, including these RBCs in the MCH calculation would have increased the measured MCH_{COM} by only 2.6% ± 1.0. This means that missed RBCs explain, at most, roughly one quarter of the decreased MCH_{COM}, which still leaves a significant difference compared to the original tests.

The same method as shown in section 4.3.4 was used to determine the impact of missed pixels on the three-day incubated test's MCH_{COM}. The bias due to missed pixels was found to be -9.7% ± 0.8, which is insignificantly different from the Experiment 1 test-to-test mean bias of 10.2%. Therefore, the lowered MCH_{COM} value found for the 3-day incubated test seems not to have been caused by sensitivity of the computer-vision algorithm to the shrunken RBC morphology.

Chapter 5: Discussion

5.1: Experiment 1

Overall, the results were encouraging. In Experiment 1, a $CV_{MCH,total}$ of 3.99% was achieved, shown by the confidence interval of [3.81,4.19] to be smaller than the 5% $CV_{MCH,target}$. As discussed in Chapter 1, $CV_{MCH,total}$ is the most important measurement target for this research because it approximates COM's $CV_{MCH,precision}$. The result indicates that COM has the potential to fulfill clinical requirements for MCH measurement. Practically speaking, the $CV_{MCH,total}$ is probably not sufficient to meet the commercial standard of $CV_{MCH,precision} < 2\%$, which would be desirable for commercial purposes. Furthermore, a smaller $CV_{MCH,total}$ may be needed to achieve a 5% CV_{target} for the MCH derivatives, i.e., Hgb and MCHC, depending on COM's performance for [RBC] and MCV, respectively. Further improvements to the MCH_{COM} measurement are likely necessary for a clinically useful or commercially viable POC-CBC machine. However, the results here represent a dramatic improvement over the previously reported microspectrophotometry-based MCH, which had a $CV_{MCH,precision}$ of 28%[27].

The regression model obtained in Experiment 1 was promising. The R^2 value of 0.886 indicates a strong linear correlation of COM with the StP, as does the very small p-value for *a*. The *a* value of 0.46 ± 0.04 indicates that COM consistently underestimates the MCH. As suggested in Chapter 2, this may be due to varying RBC thickness within pixels, as well as reflection, refraction and interference effects of the RBCs. Part of the low *a* value can also be accounted for by the -10.2% bias due to the pixels missed by thecomputer-vision algorithm. Also, the rough approximation of the extinction coefficient for met-Hb may be slightly off from the true value, in part because the wavelength profile of the LED was not precisely known.

The other fixed-effect model parameter, *b*, may be greater than 0, but more data are needed to confirm this (the p-value for this hypothesis was 0.53, greater than the standard 0.05). If $b \neq 0$, this would be due to a phenomenon that is uncorrelated with or not linearly dependent on [Hb]. Many of the model limitations discussed in Chapter 2 could fit this profile, as could the extra pixels included by the computer-vision algorithm.

Before using *a* and *b* as a correction factors for future tests, the uncertainty in both could be reduced by collecting additional data.

The $CV_{MCH,h}$ of 3.56% was substantially larger than the $CV_{MCH,\varepsilon}$ of 1.77%. The low $CV_{MCH,\varepsilon}$ suggests that the methodology used in this research was able to provide fairly consistent measurements on identical samples. This suggests that the imaging system and computer-vision algorithms performed acceptably on a test-to-test basis, though not necessarily a subject-to-subject basis. For reference, the various contributors to $CV_{MCH,total}$ referred to in this text are broken down hierarchically in Figure 16.

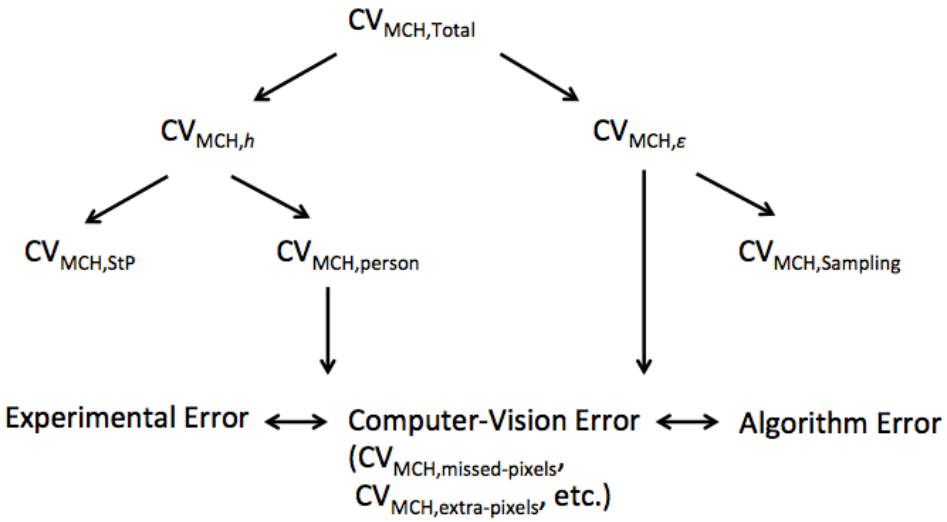

Figure 16: Breakdown of $CV_{MCH,total}$. The 2nd row indicates the $CV_{MCH,total}$ components outputted from the mixed model; the 3rd row shows further breakdowns discussed herein; the 4th row indicates the three sources of error, all of which may have contributed to both test-to-test error ($CV_{MCH,\varepsilon}$) and person-to-person error ($CV_{MCH,person}$). "Algorithm Error" refers to potential violations of the assumptions required for Equation 8.

Despite running in an interpreted programming language (MATLAB), the computer-vision algorithm produced a result in less than 20 seconds per test, meaning that it would be potentially viable for inclusion in a POC device.

Having established that the StP-error ($CV_{MCH,StP}$) contribution to $CV_{MCH,h}$ was relatively small, it seems that the main source of variation in Experiment 1 was due to person-specific blood characteristics, i.e., $CV_{MCH,person}$. It is possible that the computer-vision

algorithm's performance varied based on person-specific blood characteristics. However, the results of the missed-pixel analysis suggest that this was not the dominant factor.

5.1.1: Experiment 1 Limitations

There are some limitations on the ability of these results to support the central hypothesis.

The primary limitation was statistical in nature. The sample size for Experiment 1 was 15 subjects and 53 tests. There were only six subjects outside the StP range of 26.6-31.5 pg, compared to nine inside, leading to less confidence in the correlation outside this inner range. Including more subjects outside this range could have significantly impacted the model. The sample size of 15 is also not at all sufficient for drawing conclusions about the frequency of outliers, which would be required for a commercial device. Hundreds or thousands of tests would be required to verify and validate a potential commercial device and determine the frequency of outliers as well as any potential variations between subpopulations (sex, ethnicity, age, etc.).The correlation appeared to weaken toward the upper end of the range. The three subjects with the highest MCH_{StP} had similar MCH_{StP} values but exhibited considerably more variability in the MCH_{COM}. Two of these subjects were outliers, substantially contributing to the $CV_{MCH,person}$. For this reason, it is difficult to generalize the correlation and the model to this part of the range. Indeed, removing the three subjects in the upper range alters *a* and *b* significantly (though not drastically) and improves $CV_{MCH,total}$ significantly, as seen in Table 6.

Table 6: Experiment 1 (Diluent N) MCH statistics, with the largest three MCH_{StP} measurements excluded (Subjects 5, 10, and 15). 2nd section: N-values, R^2, CVs, *exactRLRT* p value, and measured ranges. 95% confidence intervals in square brackets.

	Estimate	Std. Error	df	t-value	p-value
b	2.061	0.9238	9.79	2.23	0.0503
a	0.4093	0.03261	9.82	12.54	$2.28*10^{-7}$

Number of Subjects	12
Number of Tests	44
R^2	0.904 [0.872,0.947]
$CV_{MCH,target}$	5%
$CV_{MCH,total}$	2.87% [2.75,2.99]
$CV_{MCH,h}$	2.15%
$CV_{MCH,\varepsilon}$	1.90%
exactRLRT p value	0.0001
Measured Range	22-31.5 pg
Required Range	24-37 pg
% of Required Range Measured	58%

One other limitation was the use of venous blood in this experiment rather than capillary blood, which would be used in a POC device. There are conflicting results in the literature[57], [58] as to whether there exists a small difference in StP-CBC measurements when using capillary blood instead of venous blood. Ultimately, COM will have to be tested with capillary blood to demonstrate its efficacy in the POC context for which it is intended.

5.2: Experiment 2

For Experiment 2, it was shown that Diluent xN can perform as well as or better than Diluent N in facilitating MCH measurement. If this had not been the case, it would have suggested that the oxy/deoxy-Hb ratio in the blood impacts the result when no nitrite is included in the diluent. Based on these data, however, it appears that nitrite is not essential for performing a COM-based MCH measurement.

5.2.1: Experiment 2 Limitations

By the time the blood mixture was injected into the specimen chamber, it had been exposed to atmospheric oxygen several times in the various blood handling steps. Therefore, it is quite plausible that all the deoxy-Hb in the venous blood had been converted to oxy-Hb prior to imaging. As a result, it cannot be concluded that the oxygenation state of the blood has no impact on the MCH measurement.

In a POC context using capillary blood, it is not known if oxygen exposure on the fingertip is sufficient for full conversion to oxy-Hb, making met-Hb conversion unnecessary. It would still be useful, though, if the device could test venous blood that had not had oxygen exposure. To explore this issue further, the experiment could be repeated, but using the original, fully-filled and sealed, venous blood-tube for both the StP and COM measurements, with care taken to minimize oxygen exposure. Chemical conversion to a single Hb species may be the preferable solution, though, to maximize the consistency of the device in face of potentially large variations in oxygen exposure in real POC contexts.

It is also interesting that the results for the subset of subjects measured for Experiment 2 produced a much stronger correlation (higher R^2) and lower $CV_{MCH,total}$. This could have been due to the fact that these were the last subjects tested, meaning the experimental operator was more experienced and performed the experiments more consistently. However, it was also likely due to the wider range of StP values relative to the total number of subjects. The smaller sample size also reduces confidence in the results.

5.3: Physical Model Limitations

Inherent limitations of the assumptions made for calculating the MCH, discussed in Chapter 2, may be crucial. To explore this, it is helpful to examine images from the outlying subjects (Subjects 5 and 10) and the non-outlier with a similar StP value, Subject 15. On average, COM underestimated Subject 5 by 6%, overestimated Subject 10 by 7%, and overestimated Subject 15 by only 3%. Figure 17 shows that the RBCs of each subject have different appearances. Subject 5 has mostly smaller RBCs with somewhat darker centers; Subjects 10 and 15, with higher MCH_{COM} values, have mostly larger

RBCs with lighter centers. This suggests that RBC shape and pattern may affect MCH_{COM} measurements, specifically that smaller and/or darker centered RBCs result in a lower COM_{MCH}.

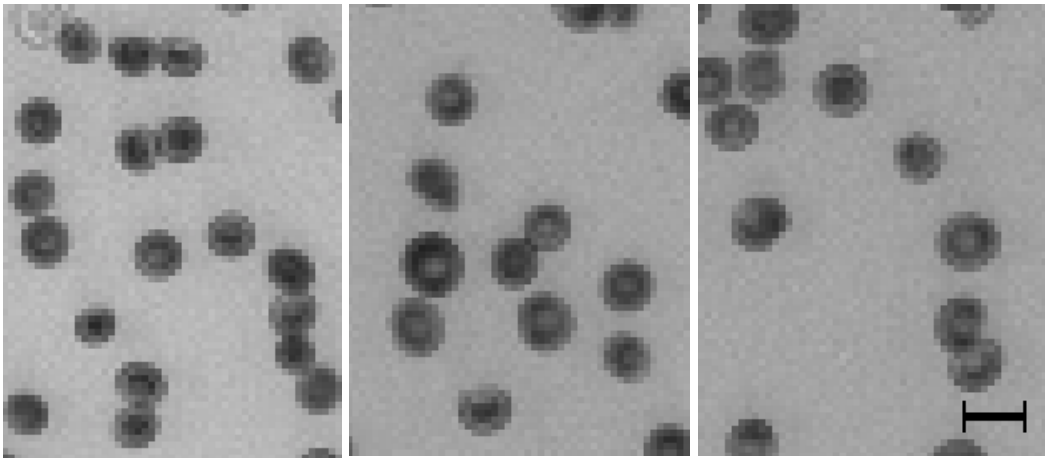

Figure 17: Morphological variations of upper-range subjects. Left: Subject 5, containing noticeably smaller RBCs. Middle: Subject 10. Right: Subject 15. Scale bar indicates 10 µm, equivalent to 9.1 pixels.

Experiment 3 was conducted to help explore model limitations. There was only one test and one time point in Experiment 3, so firm conclusions cannot be drawn from this experiment alone. It suggested, though, that the time between blood draw and COM testing had the effect of decreasing the MCH_{COM}. For the three-day test, RBCs also became smaller, with darker centers, which aligns with the observations of the Subject 5 outlier. The Subject 5 COM tests were performed several hours after the original blood draw, so it is possible that this delay resulted in the change in morphology. However, other subjects' blood underwent similar delays that did not result in shrunken appearance or reduced MCH_{COM}, so this delay alone does not explain the result for Subject 5.

One of the tests performed on Subject 8 also yields evidence that aligns with the hypothesis that shrunken RBCs result in a reduced MCH_{COM}. Figure 18 shows a section from near the lower left corner of the first and last images taken for this test.

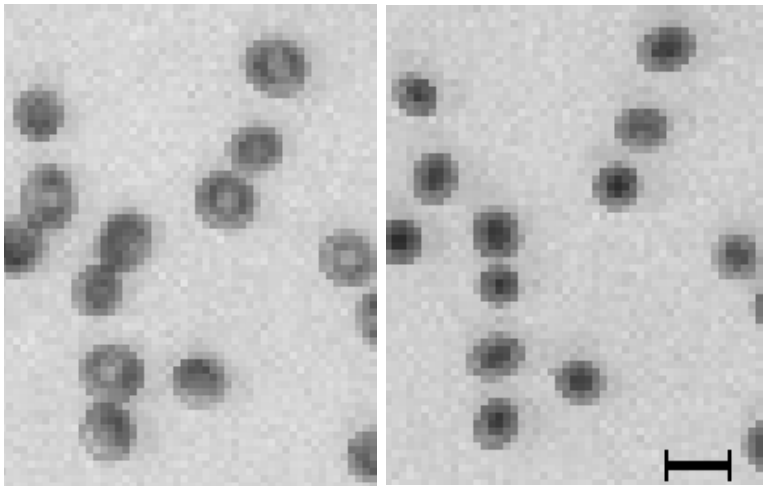

Figure 18: Shrinking RBCs from Subject 8, Test 2 bottom left region with 405 nm illumination. Left: first image. Right: last image. The time passed between the two images was roughly 18-22s. Scale bar indicates 10 µm, equivalent to 9.1 pixels.

It is clear from Figure 18 that during the 18-22s waited between the first and last images, the RBCs became noticeably smaller, with darker centers. This phenomenon only occurred in roughly $1/12^{th}$ of the field of view (a portion that was cropped for all tests in Experiment 1). The MCH algorithm was applied to this region of the first and last images. The first image yielded a model-corrected MCH of 30.7 pg while the last image yielded 25.6 pg. With sampling errors of < 10%, this decrease of 15% is significant. In other COM tests, shrinkage of most RBCs in the image was observed to occur after leaving the sample on the sensor for several minutes, producing results similar to Figure 20. Indeed, the shrunken RBCs of Subject 5 in Figure 17 may have been due to an inadvertent acceleration of this process.

Subject 5's low outlying MCH_{COM}, Subject 15's reduced MCH_{COM} after the three-day incubation (Experiment 3), and one of the Subject 8 test's MCH_{COM} decrease in part of the image all appear to correspond to smaller, dark-centered RBCs. In at least two of these cases, RBCs underwent apparent shrinkage concomitant with their reduced MCH_{COM} values, as determined by measuring the MCH_{COM} at two time points, suggesting that RBC changes over time affect the MCH_{COM} measurement. It would be undesirable if the MCH_{COM} measurement is time sensitive or dependent on individuals' RBC geometry, so it is worth exploring the possible causes of these observations.

5.3.1: Other Explanations for Reduced MCH_{COM}

There were other possible causes of the reduced MCH_{COM} to be ruled out before concluding that the cause was shrunken RBCs. First, the computer-vision algorithm does not seem to have been responsible, as the MCH_{COM} underestimation in Subjects 5, 10 and 15 due to missed pixels did not correlate with the MCH_{COM}. In any case the $CV_{MCH,missed-pixels}$ was only 1.4%, which does not account for the Subject 5 MCH_{COM} being 9% lower than the Subject 15 MCH_{COM}.

Another possibility was that the RBCs shrank due to Hb leakage. This might lower the Hb per RBC and also increase the background absorbance, leading to lowered MCH_{COM} measurements. However, Hughs et al measured serum Hb content after leaving whole blood at room temperature for 72 hours, and measured no change in serum Hb levels[59]. Also, they measured no changes in hematocrit (fraction of blood occupied by RBCs), indicating that the cells did not change volume during incubation.

Given the notable population of RBCs that began to fade into ghosts immediately before or during imaging, it is plausible that some aspect of blood-film formation had an impact on RBC structure. It is possible, therefore, that leakage occurred during or after the RBCs coming in contact with the sensor. However, as shown in Chapter 4, the ghosts themselves appeared to be a small enough population that the full leakage of their Hb would not significantly impact the MCH_{COM}.

Additionally, once RBCs shrank after a few minutes on the sensor, it was observed that they tended to be stable in appearance. If leakage was occurring, it is not clear why the shrinkage process would stop, rather than continuing toward complete ghosting. For all these reasons, it seems unlikely that increased background [Hb] was the main factor in the reduced MCH_{COM}.

Another possibility is that in the images with shrunken RBCs, the sensor temperature was considerably higher than in other images, resulting in a change in Hb absorbance. In the range of 478-585 nm, the extinction coefficient of oxy-Hb changes by up to 5% when the temperature is increased from 20ºC to 40ºC[60]; such a change might also occur around

405 nm. This change would be detectable by COM. It is plausible that that the blood-film temperature varied by 20ºC from test to test. However, because the sensor was turned off and cooled between tests, sensor temperature was likely test-independent, notwithstanding operator error. It therefore seems unlikely that a change in absorbance contributed to $CV_{MCH,person}$ or was responsible for the reduced MCH in each of the four Subject 5 tests. However, sensor-temperature variation could have been a contributor to $CV_{MCH,\varepsilon}$, which was measured as 1.77%.

The most likely remaining explanation for the observations is that the MCH_{COM} measurements depend on RBC shape, presumably due to violations of the Beer's law assumptions discussed in Chapter 2. To understand where assumptions may have been violated, it is helpful to better understand the shrinkage phenomenon.

5.3.2: Cause of Shrunken RBCs

What causes shrinkage of RBCs? The time delay between the blood draw and the COM test, during which the blood was stored at room temperature, could have led to stiffening or other morphological changes that made the RBCs more sensitive to stresses[61]. In other words, the time of *ex vivo* blood incubation before the COM test could have somehow sensitized the RBCs to some aspect of the specimen chamber.

This aspect could have been the heat given off by the OV8850. The sensor becomes hot to the touch after it is left on for a few minutes. Further insulating the sensor with the blood film and chamber lid could have led to a significant temperature increase. Christel & Little tested the morphological effects of raising RBCs to 46 ºC, 48 ºC, and 50 ºC after they had been stored *ex vivo* for various durations. This temperature range includes the transition temperature of spectrin, one of the structural support proteins in RBCs. They showed that when one-day-old whole blood is incubated at 50 ºC for 1 minute, most RBCs are converted from discocytes (the standard, biconcave-disk shape) to spherocytes (smooth spheres); however, no change occurred within the first 5 minutes of incubation at 48 ºC[61]. Spherocytes have smaller maximum diameters than discocytes. They are also thicker in their centers relative to their edges, unlike discocytes. Both of these features are consistent with the shrunken, dark-centered RBCs in the COM images, suggesting

spherocytosis as an explanation for the observations. The rapid shrinking of RBCs in Subject 8 could have occurred if heat distribution was uneven across the OV8850, leading to more rapid spherocytosis in certain regions.

On four-week-old blood, Christel & Little showed that the transition from discocyte to spherocyte or echinocyte (RBCs with bumpy protrusions and varying degrees of disk-to-sphere transition) is induced more quickly and at lower temperature (46 ºC); it is also more prevalent at 50 ºC[61]. It is difficult to compare Christel's four-week, refrigerated incubation to Experiment 3's three-day, room temperature incubation. However, this result suggests that older RBCs lose their discocyte shape more easily than fresher cells when exposed to a high temperature, which would be a possible explanation for the observation from Experiment 3. Further experiments are required to determine the effects, if any, of blood incubation times on MCH_{COM} measurements and on RBC shape in COM images.

As the temperature of the blood film on the sensor was unknown and likely varied during and between tests, it is not possible from the data available to predict exactly what happened to the RBCs' shapes in this research. However, it does seem likely that heat-induced spherocytosis led to some of the mentioned anomalies. It is possible that heat or age contributed to the smaller apparent RBCs observed for Subject 5. It is also possible either that cells from this subject were inherently susceptible to echinocytosis/ spherocytosis or that the subject's RBCs were naturally differently shaped than the other subjects' RBCs of similar MCH_{StP} values.

5.3.3: Possible Effects of RBC Shape on MCH_{COM}

The analysis in section 2.2.6 hints at possible explanations as to why spherocytosis would reduce the MCH_{COM}. It was shown in that section that the more RBC thickness (ℓ) varies within a pixel, the larger the under underestimation of $m_{Hb,p}$, with up to 40% underestimation for some RBC pixels. This effect is likely to be largest at the perimeter of RBCs, where $\ell = 0$ within part of the pixels. When an RBC becomes sphere-shaped, a higher percentage of its COM pixels are edge pixels, the center is thicker, and reflections and refractions become altered. It seems reasonable that these changes may

have combined in some way as to cause relative underestimation of the MCH. This conjecture should be quantified by explicitly modeling different RBC shapes in COM images using Mie theory.

5.3.4: Recommendations

In subsequent experiments, it may be helpful to observe the blood mixture and whole blood under a standard microscope prior to COM imaging. This would allow for higher-resolution images of the cells to help facilitate determination of their shape prior to any effects of sensor heat.

Ultimately, with a sensor that could be turned on immediately prior to imaging and a rapid (<1 second), automated imaging sequence, high sensor temperatures could be avoided, preventing potential heat-induced RBC morphology changes.

Another step that could be taken is to develop a more robust model of the absorbance of RBCs in a COM image. This would require using Mie theory, while taking into account the effects of varying ℓ within pixels. This could help to predict the expected spatial intensity distribution on the image plane of various RBC shapes and sizes. The form of the model might point to simpler correction factors for the MCH_{COM} based on easily quantified RBC properties, such as RBC area, deviation from circularity, and spatial intensity distribution within an RBC image. Even without developing such a model, some of these correction factors should be tested empirically on the COM tests from these experiments.

In future studies, the temperature of the blood film should be monitored. The temperature dependence of the extinction coefficients of oxy, deoxy, and met-Hb, as well as other diluent components, should be measured at 405 nm and 415 nm over the range of temperatures observed in COM blood films, and a temperature-dependent correction factor could then be employed potentially to improve the measurement precision.

RBC shape varying by subject may ultimately lead to difficulties in calculating the MCV and RDW using COM. This problem may also be amenable to the use of shape-based correction factors.

5.4: Computer-Vision Limitations & Recommendations

The computer-vision algorithm used in this research was based on a fairly simple conceptual design, and was intended merely to help prove the concept of a COM-based MCH measurement. The assumptions required for the background-measurement algorithm were fulfilled in the measured image region. The algorithm rarely missed or double-counted singlet RBCs. The two main drawbacks of the algorithm were missed pixels and extra pixels in the RBC segmentations. These likely led to a bias in the MCH_{COM} measurements, which would have been accounted for by the regression model. The extent to which these aspects contributed to $CV_{MCH,total}$ was characterized: the $CV_{MCH,missed\text{-}pixel}$ was found to be 1.4% and the $CV_{MCH,extra\text{-}pixel}$ was found to have a likely upper limit of 0.8%. These values were too small to account for the majority of $CV_{MCH,total}$ or $CV_{MCH,h}$, but may have accounted for the majority of $CV_{MCH,\varepsilon}$.

More thorough analyses of the algorithm's performance will eventually be required. This may involve manually counting missed and extra pixels in a larger number of RBC segmentations and a larger number of subjects and tests. This could improve the estimation of $CV_{MCH,extra\text{-}pixel}$ in particular, and allow for separation of the algorithm's contributions to $CV_{MCH,h}$ and $CV_{MCH,\varepsilon}$. However, given that there is considerable "low-hanging fruit" for improving the algorithm, it is instead recommended that such algorithmic improvements be carried out prior to more extensive evaluation.

To improve the algorithm, a thresholding method could be used that takes better advantage of the flat, pre-calculated background and the sparseness of the images. For example, a predetermined number of standard deviations below the local, estimated background value could be used as the threshold. Statistical methods could then be used to determine if pixels of intermediate intensity adjacent to RBC segmentations should also be included in that segmentation.

The algorithm could also attempt to identify objects that are not RBCs, potentially by including information from the red, blue, and green images acquired during the imaging procedure. If such objects are part of an RBC segmentation, that segmentation could be excluded from the MCH calculation, as it is likely to contain extra pixels.

Rather than simply excluding segmentations outside the area cutoff of ±1/2 the size-frequency histogram's singlets peak, the MCH calculation might also be improved by counting the RBCs in clusters. This could be done by morphological analysis of the foreground to count the number of RBCs in a cluster, for example by using a Hough transform to identify circular objects. Including all RBCs may help for subjects with a high RDW, where many of the largest or smallest RBCs might be excluded by the area cutoff. This may also help in cases where some RBCs have shrunk, such as Experiment 3.

Some of these improvements to the computer-vision algorithm may slow down the code, but rewriting the code in a faster language like C may compensate for this. Based on the performance of the current algorithm, the speed of the code does not appear to be an important concern in the near future.

5.5: Testing Limitations & Recommendations

There were some weaknesses in the experimental methods. There was little control over the time delay between the initial blood draw and the COM test. The delay could have ranged from 2 hours to 12 hours in some cases, and was not known. As suggested by Experiment 3, this could have impacted the results. This problem could be addressed in the future by collecting more information about the blood sample collection times and by testing if the delay has a detectable correlation with the MCH_{COM}. If so, the time delays will have to be controlled more carefully. All COM tests on a given subject were performed within 45 to 60 minutes of each other, so within-subject time variation is likely to have been less of an issue in these results.

The time that the blood film spent on the OV8850 before imaging commenced did vary from roughly 13-17s, and the film temperature was not controlled or measured. Measuring the sensor temperature is recommended for all future experiments. If necessary, including a low-vibration cooling system might be beneficial, though perhaps technologically challenging given the small dimensions involved. Turning on the sensor only immediately before imaging could also reduce the temperature at the time of imaging. This would require more customized image-acquisition hardware.

The background intensity became non-uniform once the blood film was loaded, increasing by ~20% toward the bottom left corner, which required the images to be cropped. Further testing should be performed to determine the source of this anomaly so it can be corrected.

The LEDs used in these experiments were not calibrated for wavelength. Deviation from their reported mean wavelengths, as well as wavelength spread, could have contributed to the small *a* values obtained, since the Hb absorbance peaks are fairly sharp. In future experiments, the LEDs should be calibrated and, if necessary, filtered to block unwanted wavelengths. The LEDs should also be tested for wavelength stability over time under normal operating conditions.

Chapter 6: Conclusion

Central Hypothesis: Using COM, the MCH can be measured as a component of a CBC, with clinically acceptable accuracy and precision, on a drop of blood.

In this research, a COM-based imaging system was designed to calculate the MCH of a blood sample by employing the principle of microspectrophotometry on intact RBCs. To do this, a microspectrophotometry equation based on Beer's law was derived, along with a computer-vision algorithm to extract the absorbance measurements from a COM image of a film of intact blood cells. A suitable illumination system was implemented, and the COM sensor was characterized, demonstrating adequate characteristics for spectrometry measurements. The system was also designed such that other CBC parameters could likely be extracted from the images. COM's performance across most of the required range of MCH measurement was compared to the StP using a mixed-effects regression model.

The results were largely encouraging. The COM system delivered an estimated R^2 of 0.89 and a $CV_{MCH,precision}$ of 4.0%, meeting the clinical-usefulness requirement of 5%. This result supports the central hypothesis.

The inclusion of nitrite in the blood diluent to convert oxy- and deoxy-Hb to met-Hb was not shown to be advantageous. However, due to likely oxygen contamination, it could not be ruled out that, as predicted by theory, the MCH_{COM} measurement is dependent on the oxygenation ratio of the blood sample.

Person-to-person variation in MCH_{COM} measurements was found to be a larger contributor to the overall error than test-to-test variation. A key source of person-to-person variation appeared to be that RBCs in some COM images were smaller and had darker centers, which was linked with reduced MCH_{COM} relative to the corresponding MCH_{StP}. This appeared to be caused, least in some cases, by spherulization of the RBCs, likely induced by a combination of heat from the COM sensor and *ex vivo* incubation time. Regardless of the cause, it does appear that RBC shape variations contribute to the MCH_{COM} measurement. This is undesirable unless they can be avoided or corrected for.

Overall, this research validates a key component of a COM-based, POC-CBC device. The results also suggest the potential for using COM as a platform for other types of microspectrophotometry.

6.1: Future Directions

Generally, the COM system and the experimental process need to be simplified in order to have a device that could be used in a POC setting. This may also help in reducing test-to-test variation in the MCH_{COM} measurement.

To avoid spherulization, improvements to the experimental procedure may be required. A temperature sensor should be used to monitor the blood film and test the heating-induced spherulization hypothesis. If this hypothesis is supported, the imaging system should be refined such that excessive heat build-up in the blood film is avoided. This hypothesis should also be tested using high-resolution standard microscopy prior to COM imaging to determine if prior spherulization can occur. If the problem cannot be avoided, models or correction factors could be developed to compensate for RBC morphology. Regardless, correction factors for the MCH measurement based on RBC area or other RBC image characteristics should be explored, as guided by Mie theory and by experimentation.

After some of these improvements have been made, a larger number of subjects should be tested, covering a wider StP range without sparsity within subranges. A clinical trial using capillary blood is required to fully validate the technology for POC use. Capillary blood should be tested with and without met-Hb conversion to determine if nitrite inclusion in the diluent is necessary. With MCH shown to be obtainable using COM, the other CBC parameters should be extracted from current and future datasets for comparison to the StP in order to obtain a baseline for performance. Overall, based on the encouraging results obtained herein, research into a COM-based, POC CBC should continue.

References

[1] "Canada's health care spending growth slows," *Canadian Institute for Health Information*, 2012. [Online]. Available: http://www.cihi.ca/CIHI-ext-portal/internet/EN/document/spending+and+health+workforce/spending/release_30oct12. [Accessed: 14-Jan-2015].

[2] E. Aguilera-Herrador, M. Cruz-Vera, and M. Valcárcel, "Analytical connotations of point-of-care testing," *Analyst*, vol. 135, no. 9, pp. 2220–32, Sep. 2010.

[3] N. Beck, *Diagnostic Hematology*. London: Springer London, 2009.

[4] "Blood counts," *Non-Hogkin's Lymphoma Cyberfamily*. [Online]. Available: http://www.nhlcyberfamily.org/bloodcounts.htm. [Accessed: 17-Oct-2012].

[5] "Complete blood count (CBC)," *Mayo Clinic*, 2014. [Online]. Available: http://www.mayoclinic.com/health/complete-blood-count/MY00476/DSECTION=results. [Accessed: 14-Jan-2015].

[6] M. Buttarello and M. Plebani, "Automated blood cell counts: state of the art.," *Am. J. Clin. Pathol.*, vol. 130, no. 1, pp. 104–16, Jul. 2008.

[7] Personal Communication from Hayley Parsons, Technical Specialist - Routine Haematology, QE II Health Sciences Centre, 2014.

[8] "ISO 15725-1: Accuracy (trueness and precision) of measurement methods and results - Part 1: Introduction and basic principles," 2011.

[9] D. Heikali and D. Di Carlo, "A Niche for Microfluidics in Portable Hematology Analyzers," *J. Assoc. Lab. Autom.*, vol. 15, no. 4, pp. 319–28, Aug. 2010.

[10] A. P. Tan, J. S. Dudani, A. Arshi, R. J. Lee, H. T. K. Tse, D. R. Gossett, and D. Di Carlo, "Continuous-flow cytomorphological staining and analysis," *Lab Chip*, vol. 14, no. 3, pp. 522–31, Dec. 2013.

[11] K. C. Cheung, M. Di Berardino, G. Schade-Kampmann, M. Hebeisen, A. Pierzchalski, J. Bocsi, A. Mittag, and A. Tárnok, "Microfluidic impedance-based flow cytometry," *Cytometry. A*, vol. 77, no. 7, pp. 648–66, Jul. 2010.

[12] C. van Berkel, J. D. Gwyer, S. Deane, N. G. Green, N. Green, J. Holloway, V. Hollis, and H. Morgan, "Integrated systems for rapid point of care (PoC) blood cell analysis," *Lab Chip*, vol. 11, no. 7, pp. 1249–55, May 2011.

[13] H. Zhu, I. Sencan, J. Wong, S. Dimitrov, D. Tseng, K. Nagashima, and A. Ozcan, "Cost-effective and rapid blood analysis on a cell-phone," *Lab Chip*, vol. 13, no. 7, pp. 1282–8, Apr. 2013.

[14] "White Blood Cell Count," *Hemocue*. [Online]. Available: http://www.hemocue.com/en/products/white-blood-cell-count/wbc-system. [Accessed: 14-Jan-2015].

[15] Z. Göröcs and A. Ozcan, "On-chip biomedical imaging," *IEEE Rev. Biomed. Eng.*, vol. 6, pp. 29–46, Jan. 2013.

[16] G. Zheng, "Chip-scale microscopy imaging," *J. Biophotonics*, vol. 649, no. 8, pp. 639–49, May 2012.

[17] H. J. Kreuzer, N. Pomerleau, K. Blagrave, and M. H. Jericho, "Digital in-line holography with numerical reconstruction," in *International Conference on Optical Metrology*, 1999, pp. 65–74.

[18] H. Ji, D. Sander, A. Haas, and P. a. Abshire, "Contact Imaging: Simulation and Experiment," *IEEE Trans. Circuits Syst. I Regul. Pap.*, vol. 54, no. 8, pp. 1698–710, Aug. 2007.

[19] T. Kobayashi, H. Tamura, Y. Hatanaka, M. Motoyama, T. Noda, K. Sasagawa, T. Tokuda, Y. Ishikawa, S. Shiosaka, and J. Ohta, "Functional neuroimaging by using an implantable CMOS multimodal device in a freely-moving mouse," *Sci. Technol.*, pp. 110–3, 2011.

[20] S. Farsiu, M. D. Robinson, M. Elad, and P. Milanfar, "Fast and robust multiframe super resolution," *IEEE Trans. image Process.*, vol. 13, no. 10, pp. 1327–44, Oct. 2004.

[21] G. Zheng, S. Ah, Y. Antebi, M. B. Elowitz, and C. Yang, "The ePetri dish, an on-chip cell imaging platform based on subpixel perspective sweeping microscopy (SPSM)," *PNAS*, vol. 108, no. 41, 2011.

[22] G. Zheng, S. A. Lee, S. Yang, and C. Yang, "Sub-pixel resolving optofluidic microscope for on-chip cell imaging," *Lab Chip*, vol. 10, no. 22, pp. 3125–9, Nov. 2010.

[23] S. A. Lee, R. Leitao, G. Zheng, S. Yang, A. Rodriguez, and C. Yang, "Color capable sub-pixel resolving optofluidic microscope and its application to blood cell imaging for malaria diagnosis," *PLoS One*, vol. 6, no. 10, Jan. 2011.

[24] W. Bishara, T.-W. Su, A. F. Coskun, and A. Ozcan, "Lensfree on-chip microscopy over a wide field-of-view using pixel super-resolution," *Opt. Express*, vol. 18, no. 11, May 2010.

[25] C. A. Sondhaus and B. Thorell, "Microspectrophotometric Determination of Nonheme Iron in Maturing Erythroblasts and its Relationship to the Endocellular Hemoglobin Formation," *Blood*, vol. 16, no. 3, pp. 1285–97, 1960.

[26] K. Tsujita, T. Shiraishi, and K. Kakinuma, "Microspectrophotometry of nitric oxide-dependent changes in hemoglobin in single red blood cells incubated with stimulated macrophages," *J. Biochem.*, vol. 122, no. 2, pp. 264–70, Aug. 1997.

[27] J. Meletis, X. Yataganas, G. Eliopoulos, J. Panourgais, D. Loukopoulos, and P. Fessas, "Hemoglobin Content of Single Erythrocytes from Fetuses with Parents Having Heterozyhous ß-Thalassemia," *Acta Haematol.*, vol. 73, pp. 16–21, 1985.

[28] "Nikon MicroscopyU | Interactive Java Tutorials | Depth of Field Calculator." [Online]. Available: http://www.microscopyu.com/tutorials/java/depthoffield/. [Accessed: 20-Nov-2014].

[29] K. G. Engström and E. Löfvenberg, "Treatment of Myeloproliferative Disorders With Hydroxyurea: Effects on Red Blood Cell Geometry and Deformability," *Blood*, vol. 91, no. 10, pp. 3986–3991, 1998.

[30] A. Beer, "Bestimmung der Absorption des rothen Lichts in farbigen Flüssigkeiten," *Ann. Phys.*, vol. 162, no. 5, pp. 78–88, 1852.

[31] A. B. Blood and G. G. Power, "In vitro and in vivo kinetic handling of nitrite in blood: effects of varying hemoglobin oxygen saturation," *Am. J. Physiol. Heart Circ. Physiol.*, vol. 293, pp. H1508–17, Sep. 2007.

[32] S. Prahl, "Optical Absorption of Hemoglobin," *Oregon Medical Laser Center*, 1999. [Online]. Available: http://omlc.org/spectra/hemoglobin/. [Accessed: 15-Feb-2013].

[33] P. K. Swain and D. Cheskis, "Back-Illuminated Image Sensors Come to the Forefront," *Photonics Spectra*, 2008. [Online]. Available: http://www.photonics.com/Article.aspx?AID=34685. [Accessed: 25-Mar-2015].

[34] M. AlMulla, A. W. Agab, L. S. Almannai, and F. Z. Henari, "Visible and Near Infrared Absorption Properties of Blood From Sickle Cell Patients and Normal Individuals," *R. Coll. Surg. Irel. Student Med. J.*, vol. 4, pp. 82–83, 2011.

[35] C. Donadee, N. J. H. Raat, T. Kanias, J. Tejero, J. S. Lee, E. E. Kelley, X. Zhao, C. Liu, H. Reynolds, I. Azarov, S. Frizzell, E. M. Meyer, A. D. Donnenberg, L. Qu, D. Triulzi, D. B. Kim-Shapiro, and M. T. Gladwin, "Nitric oxide scavenging by red blood cell microparticles and cell-free hemoglobin as a mechanism for the red cell storage lesion," *Circulation*, vol. 124, no. 4, pp. 465–76, Jul. 2011.

[36] R. Grubina, Z. Huang, S. Shiva, M. S. Joshi, I. Azarov, S. Basu, L. a Ringwood, A. Jiang, N. Hogg, D. B. Kim-Shapiro, and M. T. Gladwin, "Concerted nitric oxide formation and release from the simultaneous reactions of nitrite with deoxy- and oxyhemoglobin," *J. Biol. Chem.*, vol. 282, no. 17, pp. 12916–27, Apr. 2007.

[37] Y. Park, M. Diez-silva, G. Popescu, G. Lykotrafitis, W. Choi, and M. S. Feld, "Refractive index maps and membrane dynamics of human red blood cells parasitized by Plasmodium falciparum," *PNAS*, vol. 105, no. 37, 2008.

[38] A. J. Cox, A. J. DeWeerd, and J. Linden, "An experiment to measure Mie and Rayleigh total scattering cross sections," *Am. J. Phys.*, vol. 70, no. 6, pp. 620–5, 2002.

[39] J. K. Armstrong, R. B. Wenby, H. J. Meiselman, and T. C. Fisher, "The hydrodynamic radii of macromolecules and their effect on red blood cell aggregation," *Biophys. J.*, vol. 87, no. 6, pp. 4259–70, Dec. 2004.

[40] D. W. Hahn, "Light Scattering Theory," 2009. [Online]. Available: http://plaza.ufl.edu/dwhahn/Rayleigh and Mie Light Scattering.pdf. [Accessed: 14-Jan-2015].

[41] D. Yim, "CLBlood : A Cell-Based Light Interaction Model for Human Blood," University of Waterloo, 2012.

[42] A. Airinei and A. Sadoveanu, "Spectrophotometric Analysis of the Blood Plasma," *Rom. J. Biophys.*, vol. 16, no. 3, pp. 215–20, 2006.

[43] M. De, S. Rana, H. Akpinar, O. R. Miranda, R. R. Arvizo, U. H. F. Bunz, and V. M. Rotello, "Sensing of proteins in human serum using conjugates of nanoparticles and green fluorescent protein," *Nat. Chem.*, vol. 1, no. September, pp. 461–5, 2009.

[44] N. Na, J. Ouyang, Y. E. C. Taes, and J. R. Delanghe, "Serum free hemoglobin concentrations in healthy individuals are related to haptoglobin type," *Clin. Chem.*, vol. 51, no. 9, pp. 1754–5, Sep. 2005.

[45] M. Adamzik, T. Hamburger, F. Petrat, J. Peters, H. de Groot, and M. Hartmann, "Free hemoglobin concentration in severe sepsis: methods of measurement and prediction of outcome," *Crit. Care*, vol. 16, no. 4, Jul. 2012.

[46] D. J. Schaer, P. W. Buehler, A. I. Alayash, J. D. Belcher, and G. M. Vercellotti, "Hemolysis and free hemoglobin revisited: exploring hemoglobin and hemin scavengers as a novel class of therapeutic proteins," *Blood*, vol. 121, no. 8, pp. 1276–84, Feb. 2013.

[47] R. Glaser, "The shape of red blood cells as a function of membrane potential and temperature," *J. Membr. Biol.*, vol. 51, no. 3–4, pp. 217–28, Sep. 1979.

[48] N. Patel, "Why is EDTA the anticoagulant of choice for hematology use?," *Tech Talk - Becton Dickinson Global Technical Services*, vol. 7, no. 1, 2009.

[49] Y. Park, C. a Best, T. Auth, N. S. Gov, S. a Safran, G. Popescu, S. Suresh, and M. S. Feld, "Metabolic remodeling of the human red blood cell membrane," *PNAS*, vol. 107, no. 4, pp. 1289–94, Jan. 2010.

[50] P. Baranski, "gaussfit.m," 2012. [Online]. Available: http://www.mathworks.com/matlabcentral/fileexchange/35122-gaussian-fit. [Accessed: 14-Jan-2015].

[51] N. Otsu, "A Threshold Selection Method from Gray-Level Histograms," *IEEE Trans. Syst. Man. Cybern.*, vol. 9, no. 1, pp. 62–6, 1979.

[52] S. Nakagawa and H. Schielzeth, "A general and simple method for obtaining R_2 from generalized linear mixed-effects models," *Methods Ecol. Evol.*, vol. 4, no. 2, pp. 133–42, Feb. 2013.

[53] D. M. Bates, "lme4: Mixed-effects modeling with R." Springer, 2010.

[54] H.-T. Thai, F. Mentré, N. H. G. Holford, C. Veyrat-Follet, and E. Comets, "A comparison of bootstrap approaches for estimating uncertainty of parameters in linear mixed-effects models," *Pharm. Stat.*, vol. 12, no. 3, pp. 129–40, 2013.

[55] J. M. Bland and D. G. Altman, "Statistical Methods for Assessing Agreement Between Two Methods of Clinical Measurement," *Lancet*, vol. 327, no. 8476, pp. 307–310, 1986.

[56] W. Rasband, "ImageJ," US National Institutes of Health, Bethesda, Maryland, imagej.nih.gov/ij/, 1997-2015.

[57] E. Schalk, M. U. Heim, M. Koenigsmann, K. Jentsch-Ullrich, "Use of capillary blood count parameters in adults," *Vox Sang*, vol. 93, no. 4, pp. 348-53, 2007.

[58] S. C. Lee and L. Y. Tsai, "Blood routine tests in capillary blood compared to those of venous blood," *Kaohsiung J. Med. Sci.*, vol. 5, no. 8, pp. 471–5, Aug. 1989.

[59] J. D. Hughes, V. W. Macdonald, and J. R. Hess, "Warm storage of whole blood for 72 hours," *Transfusion*, vol. 47, no. 11, pp. 2050–6, Nov. 2007.

[60] D. Seidel and M. Steinke, "Eftects of Temperature on Optical Absorbance Spectra of Oxy- , Carboxy- , and Deoxyhemoglobin," *Clin. Chem.*, vol. 38, no. 7, pp. 1360–1364, 1992.

[61] S. Christel and C. Little, “Morphological changes during heating of erythrocytes from stored human blood,” *J. Therm. Biol.*, vol. 9, no. 3, pp. 221–8, Jul. 1984.